The Abdus Salam
International Centre for Theoretical Physics

United Nations
Educational, Scientific and
Cultural Organization

IAEA
International Atomic Energy Agency

SMR/1837-7

2007 ICTP Oceanography Advanced School

30 April - 11 May, 2007

Role of the intermediate water in the ocean thermohaline circulation

V. Artale
ENEA C.R. Casaccia, Rome
I t a l y

Role of the intermediate water in the ocean thermohaline circulation

Vincenzo Artale

C.R. Casaccia, Rome, Italy

Part one

Ocean semplified model :

1. Box model
2. 2D model

- The world oceans are an essential component of the physical climate system

- The ocean is responsible for about half of the total heat flux from low to high latitudes, that is necessary to compensate for the radiation imbalance between the equator and the poles

- The oceans act as formidable buffers that can store large amounts of heat and elements like a carbon

- To represent the ocean from a climate point of view we use ocean models

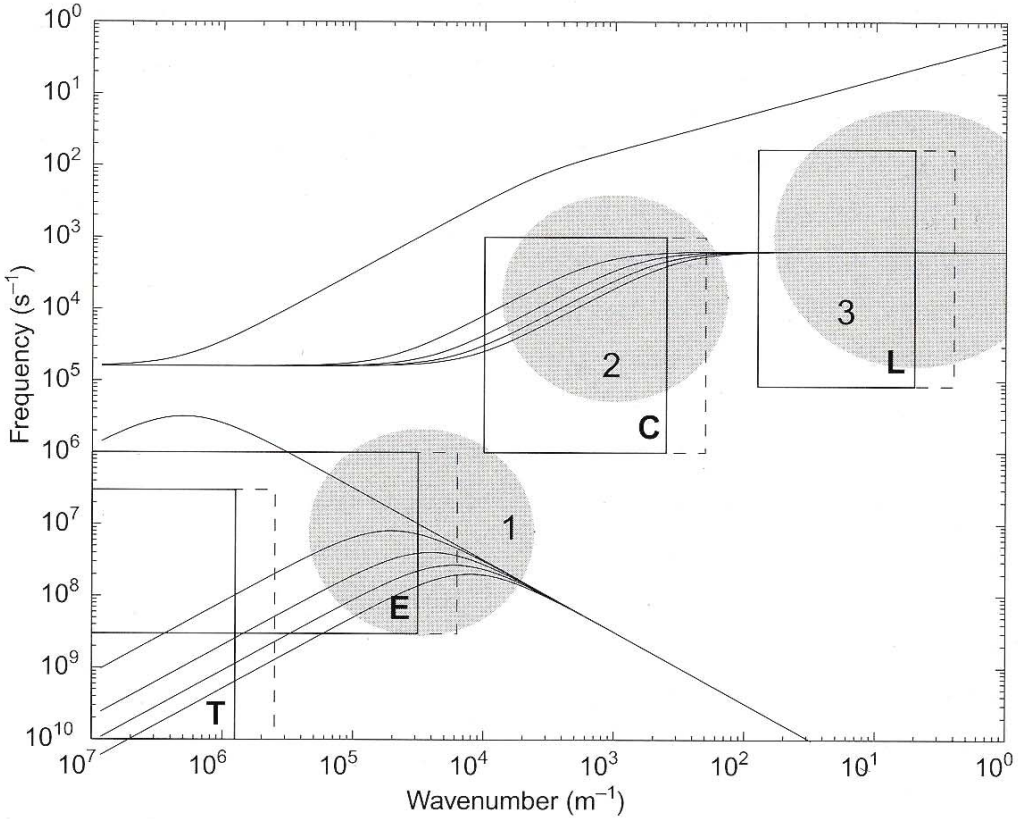

Fig. 7.2.1 Space–time scales covered by ocean models. Rectangles indicate the temporal and spatial (horizontal) scale range explicitly resolved by current ocean models: T, ocean climate models; E, global eddy-resolving models; C, ocean convection models; L, large eddy simulation of ocean mixed layer. The dashed lines indicate the expected gain in resolution within 6 years, based on an assumed doubling of CPU speed every 18 months. The thin lines are dispersion curves for linear gravity waves (upper set) and planetary waves (lower set). Each set displays the barotropic and the first four baroclinic modes, for typical mid-latitude conditions. The shaded circles give an indication of some relevant processes that are not resolved in most ocean models: 1, eddies/fronts/western boundary currents; 2, organized deep-ocean convection; 3, three-dimensional turbulence.

Our approach

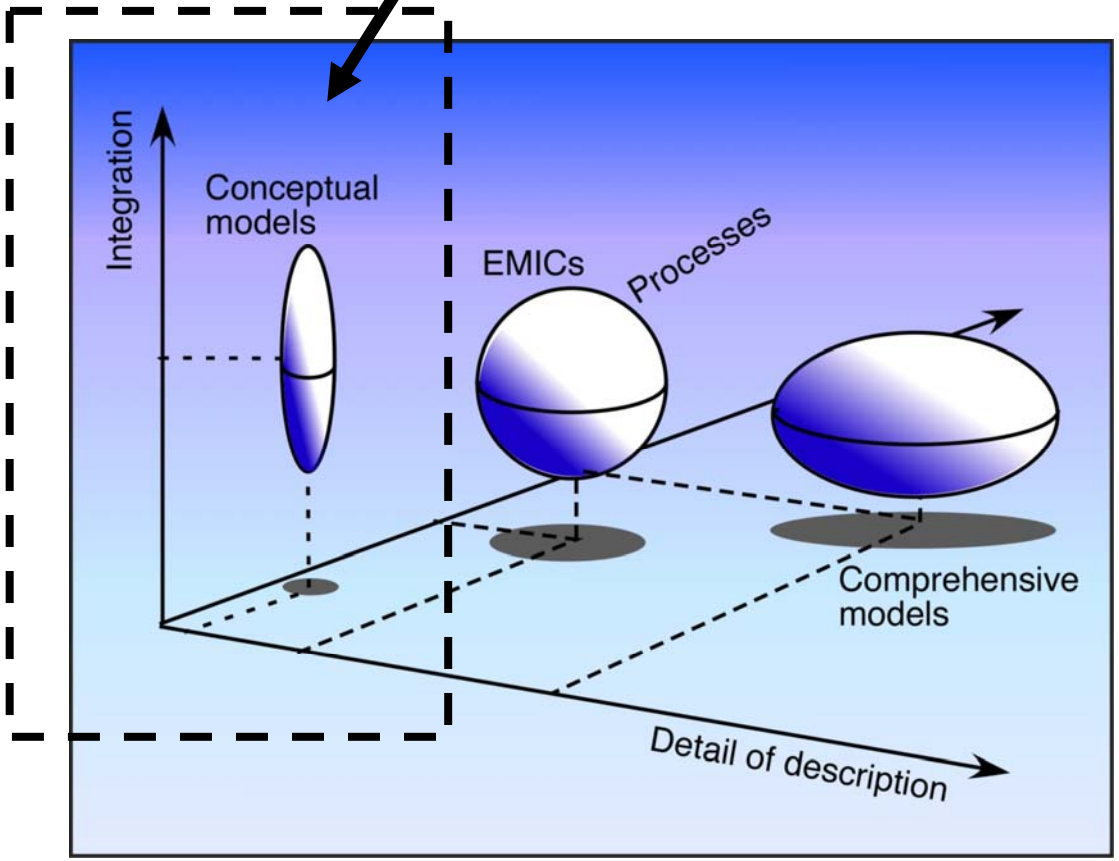

On the global scale the ocean circulation is driven by

- Wind forcing
- Fluxes of heat and fresh-water through the ocean surface (**thermohaline circulation**)

EXTERNAL FORCING
(radiative forcing)

WARM
SALT

COLD
FRESH

ATMOSPHERE
E-P AND Q

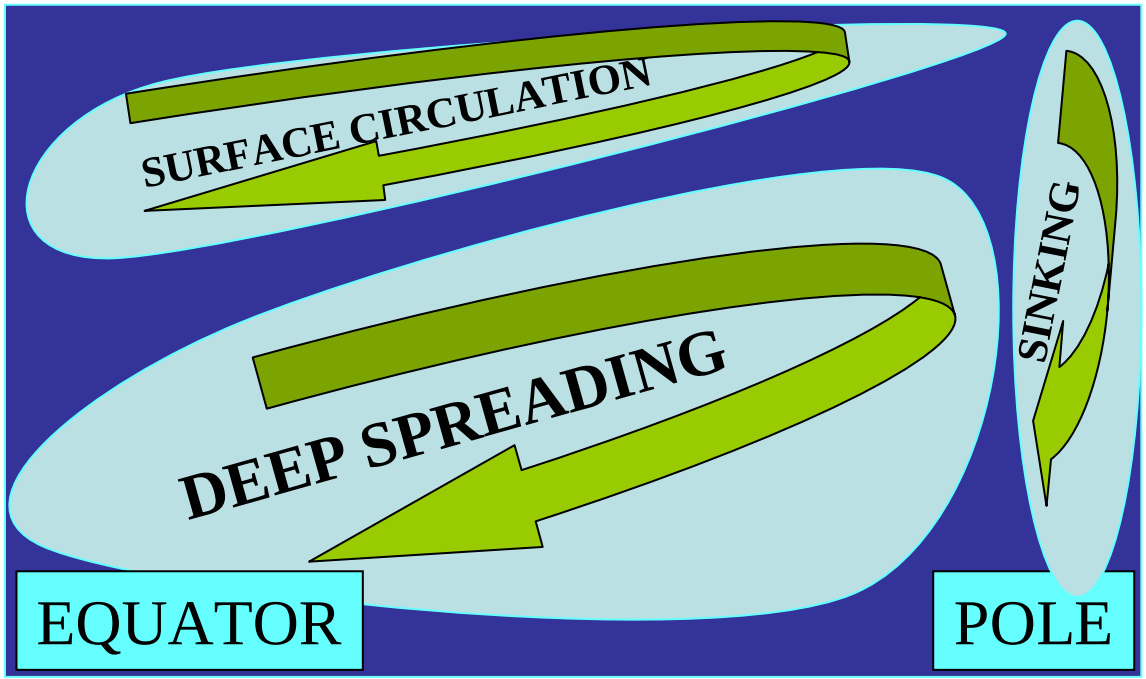

OCEAN

Wind driven circulation

- the frictionally induced wind driven circulation that tend to create upper level oceanic horizontal flows in the direction of the mean surface winds

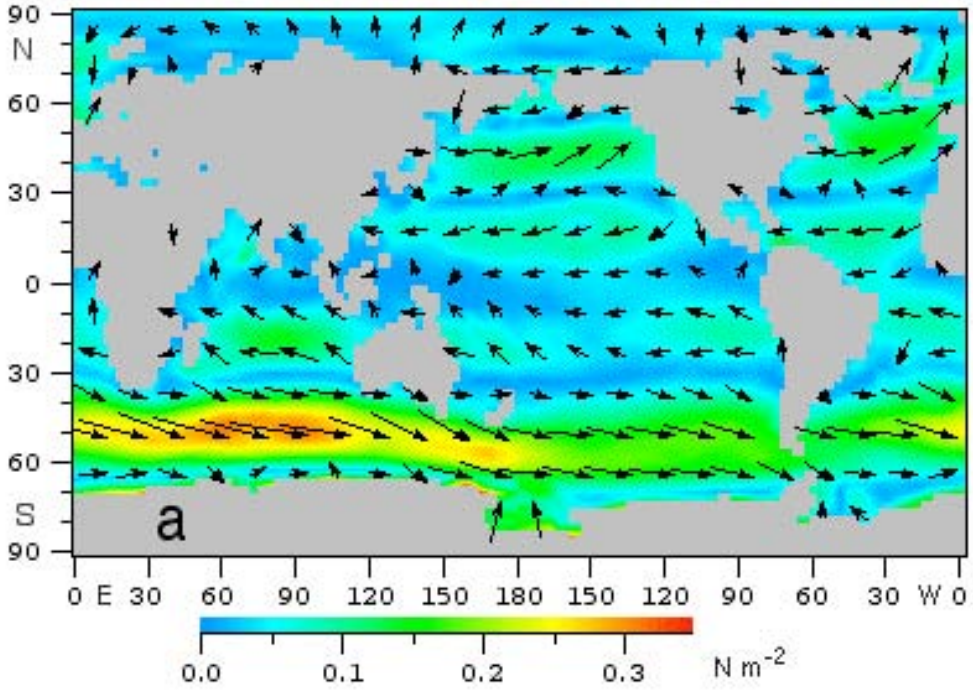

Fig. 1.4 Wind stress over the World Ocean. (a) Annual mean, (b, page 9) June - August, (c, page 9) December - February. Data from http://ferret.wrc.noaa.gov/fbs/, the NOAA Live Climate Data Server using the Trenberth *et al.* (1989) climatology. Colour indicates wind stress magnitude.

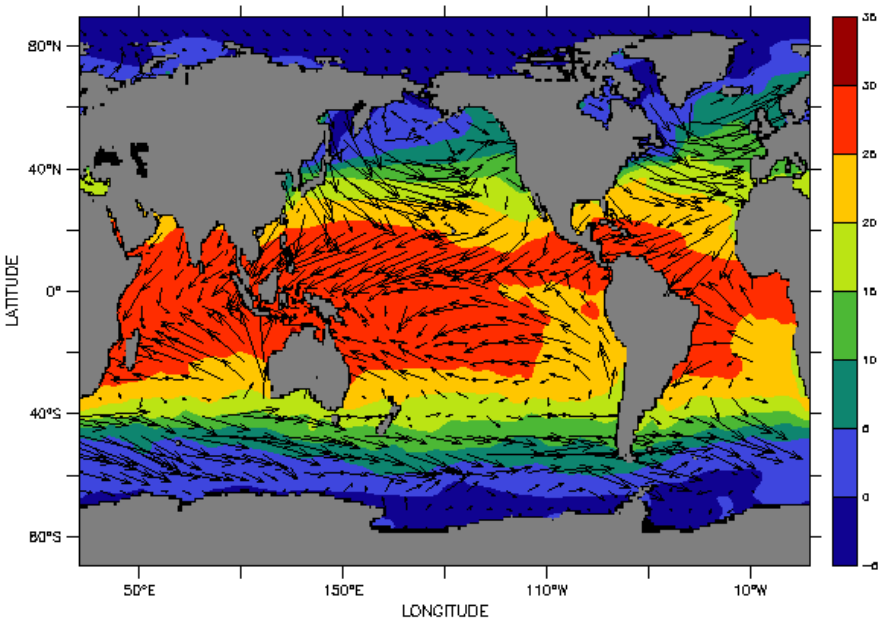

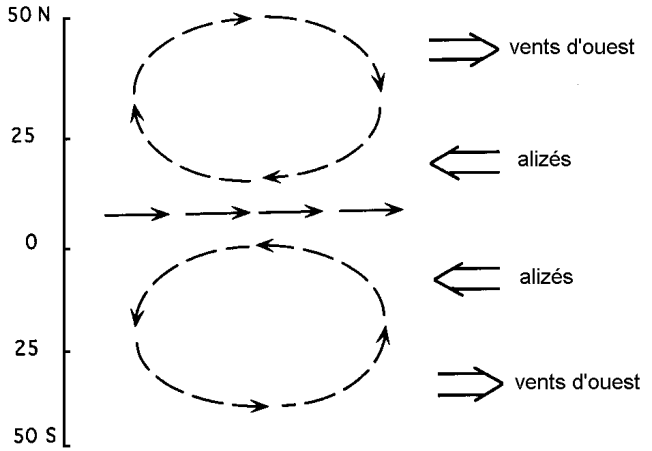

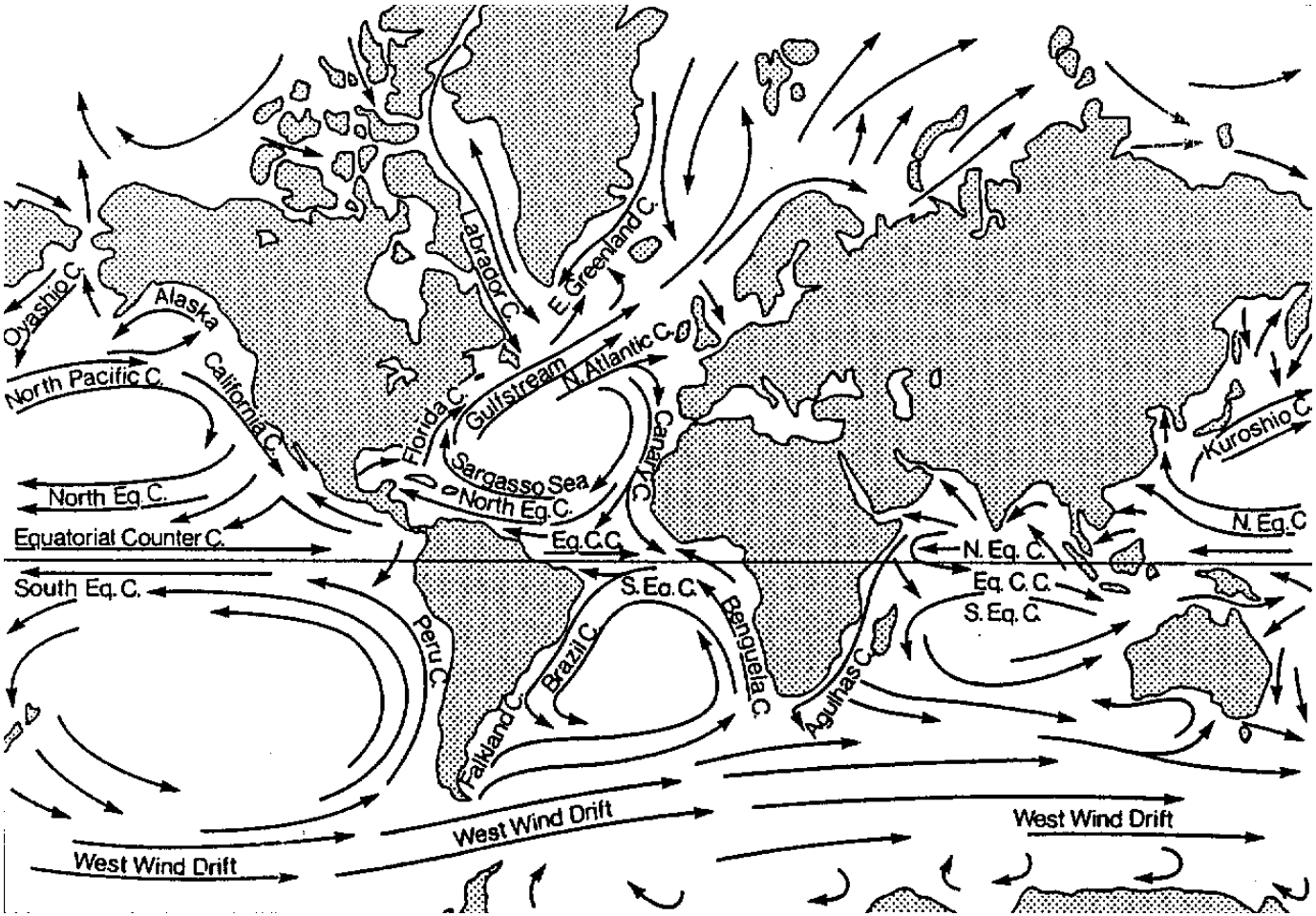
Oyashio C.
Alaska
North Pacific C.
California C.
North Eq. C.
Equatorial Counter C.
South Eq. C.
Peru C.
Labrador C.
E. Greenland C.
Florida C.
Gulfstream
N. Atlantic C.
Sargasso Sea
North Eq. C.
Canary C.
Eq. C. C.
S. Eq. C.
Brazil C.
Falkland C.
Benguela C.
Agulhas C.
N. Eq. C.
Eq. C. C.
S. Eq. C.
Kuroshio C.
N. Eq. C
West Wind Drift
West Wind Drift
West Wind Drift

Thermohaline circulation

- The component of the flow driven by horizontal pressure forces resulting from hydrostatically balanced horizontal density differences

Salinity and temperature distribution (at intermediate level)

temperature and salinity at a pressure of **1000 dbar**.

Note the large salinities in the North Atlantic and NW Indian Oceans: these are due to outflows from the **Mediterranean and Red Seas**, respectively.

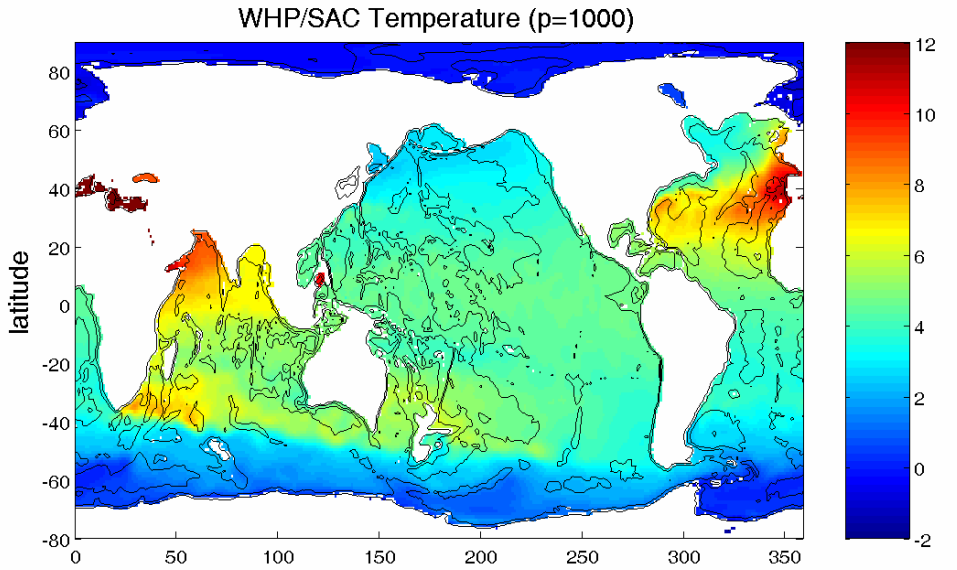

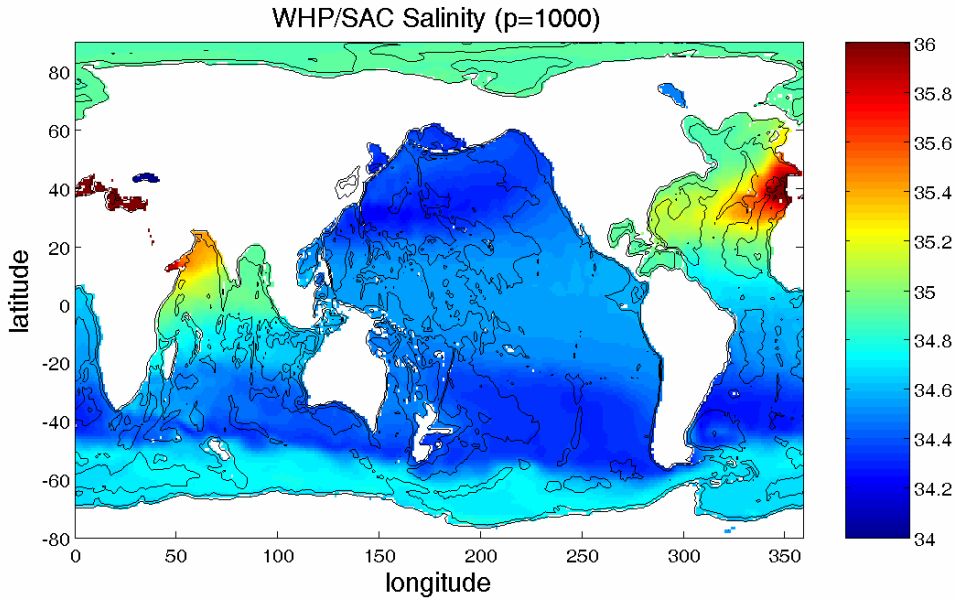

WOCE hydrographic Atlas

It is often common to plot properties on density surfaces, in order to see water mass structure. We have used neutral density surfaces for this exercise. Neutral surfaces will vary for a fixed pressure because of geostrophic flow in the ocean. At the right are plotted neutral density at the surface and at 1000 dbar.

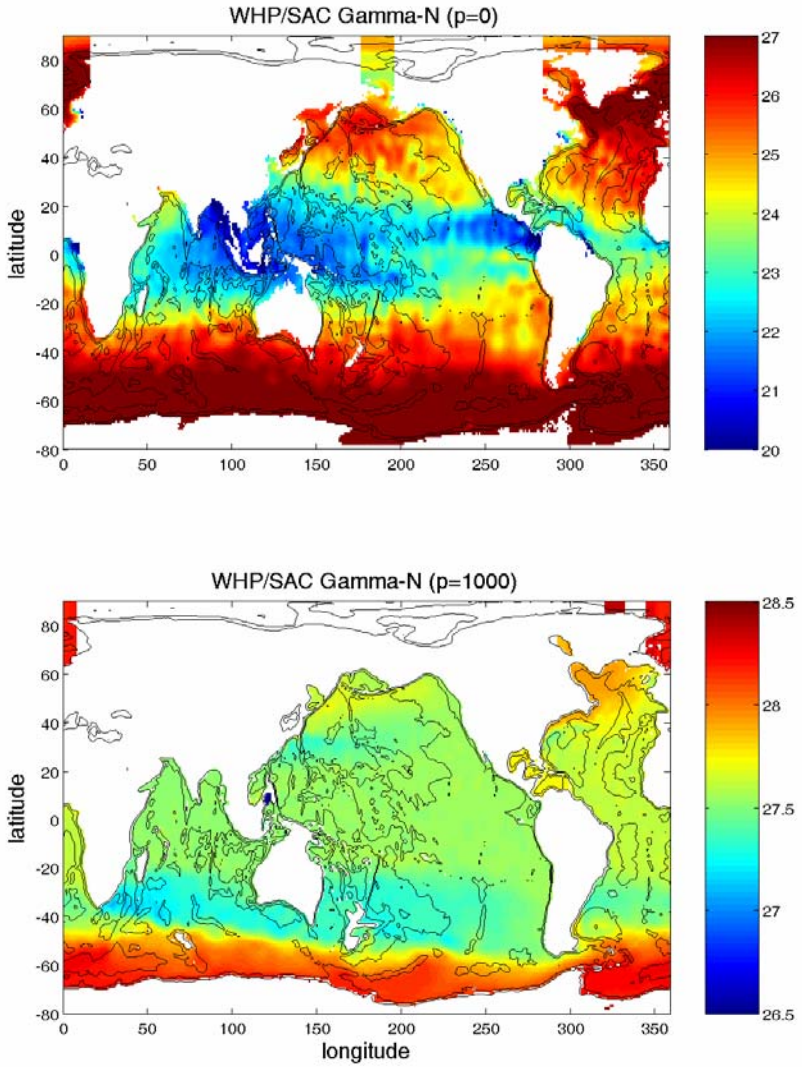

pressure (top) and salinity (bottom) on the neutral density of 27.3.

This density is one which rises to the surface (outcrops) in the Southern Ocean and is a good level for tracing properties of **Antarctic Intermediate Water** (AAIW).

We can also see effects of the **Red Sea and Med Outflows**.

Note how this display shows a much broader salty Med ‘tongue’ than on the 1000 dbar pressure level.

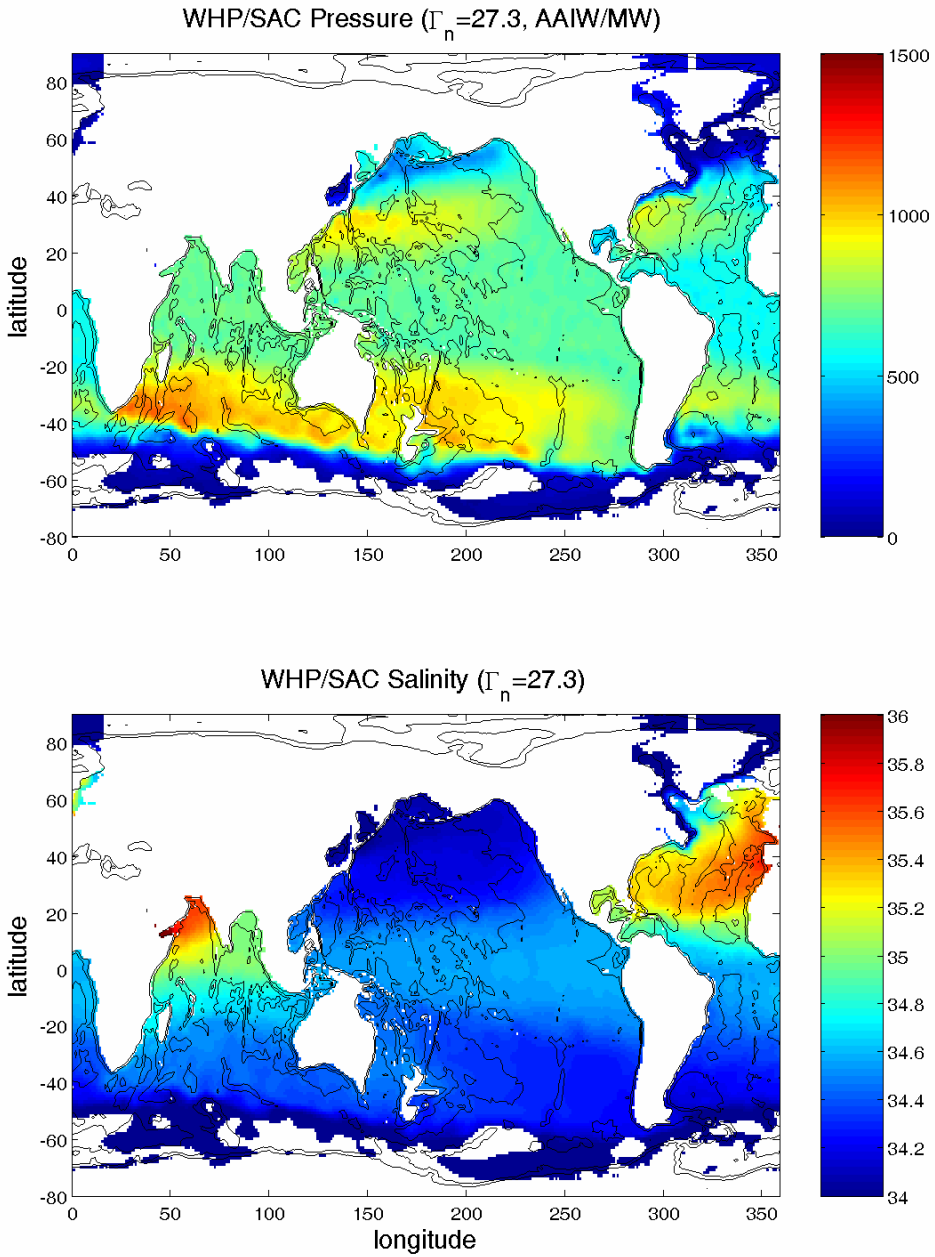

From WOCE hydrographic Atlas

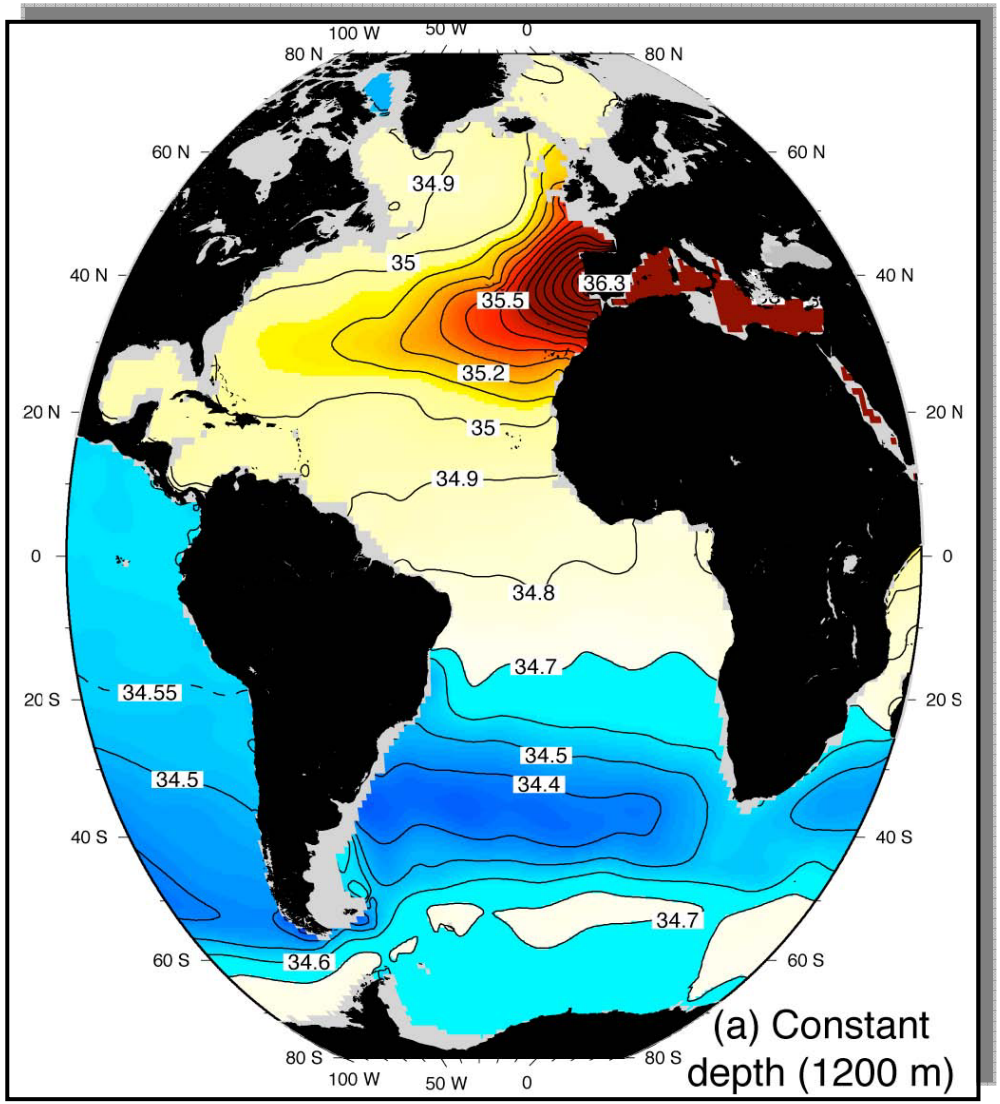
100 W
50 W
0
80 N
60 N
40 N
20 N
0
20 S
40 S
60 S
80 S
34.9
35
35.5
36.3
35.2
34.8
34.7
34.55
34.5
34.4
34.6
(a) Constant depth (1200 m)

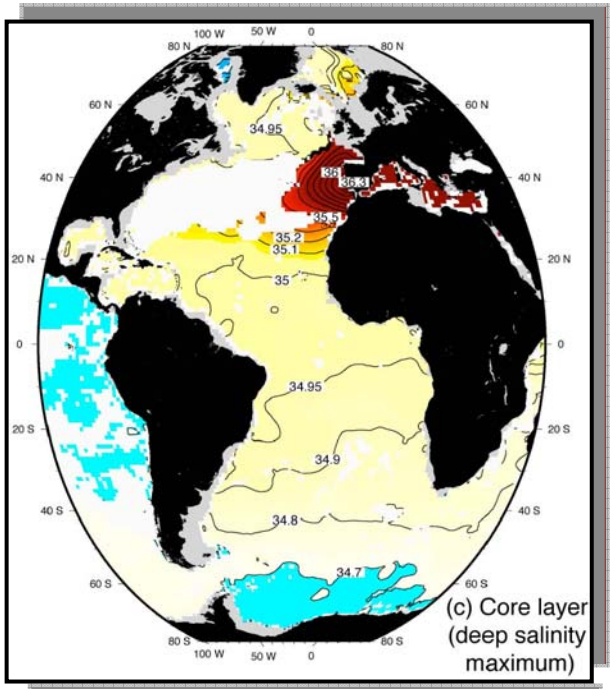
34.95
35.2
35.1
35
34.9
34.8
34.7
(c) Core layer (deep salinity maximum)

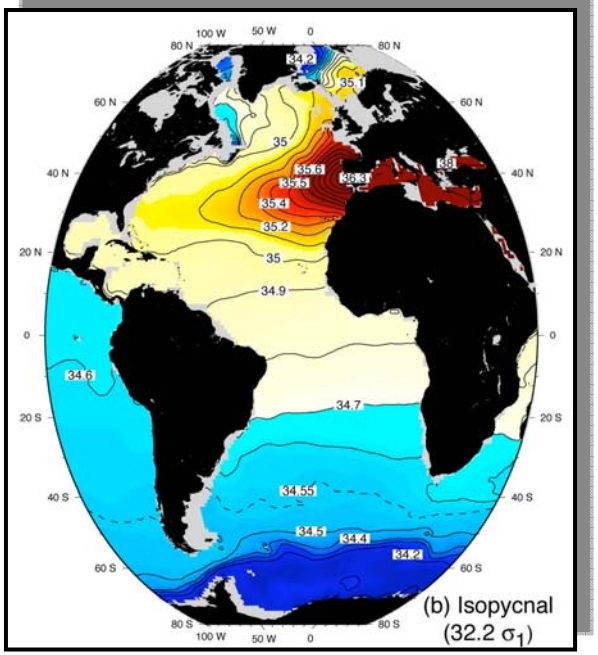
34.2
35.1
35
35.6
35.5
35.4
35.2
34.9
34.6
34.7
34.55
34.5
34.4
(b) Isopycnal (32.2 σ_1)

The fundamental processes for the TH variability

Deep water formation

- In addition to the large-scale hydrostatic TH circulation, relatively intense localized buoyancy-driven (i.e. nonhydrostatic) convective circulation cells induced by unstable vertical gradients of density, particularly in high latitude where strong surface cooling and avaporation can occur

- These area are located at high latitudes in particular in Greenland sea, Labrador sea and Weddel sea

- Mediterranean sea (Gulf of Lions)

- Red sea

- Change in the deep water prodution have a large scale response in the thermohaline circulation
- The physics of the deep-water formation is poorly understood: for example the sensitivity of the amount of deep and intermediate water to changes in the ocean-atmosphere heat flux

- Deep water is formed by cooling of the upper layer followed by an overturning of the water column
- Adjusts on a larger scale to its neutrally level
- Transported by advection

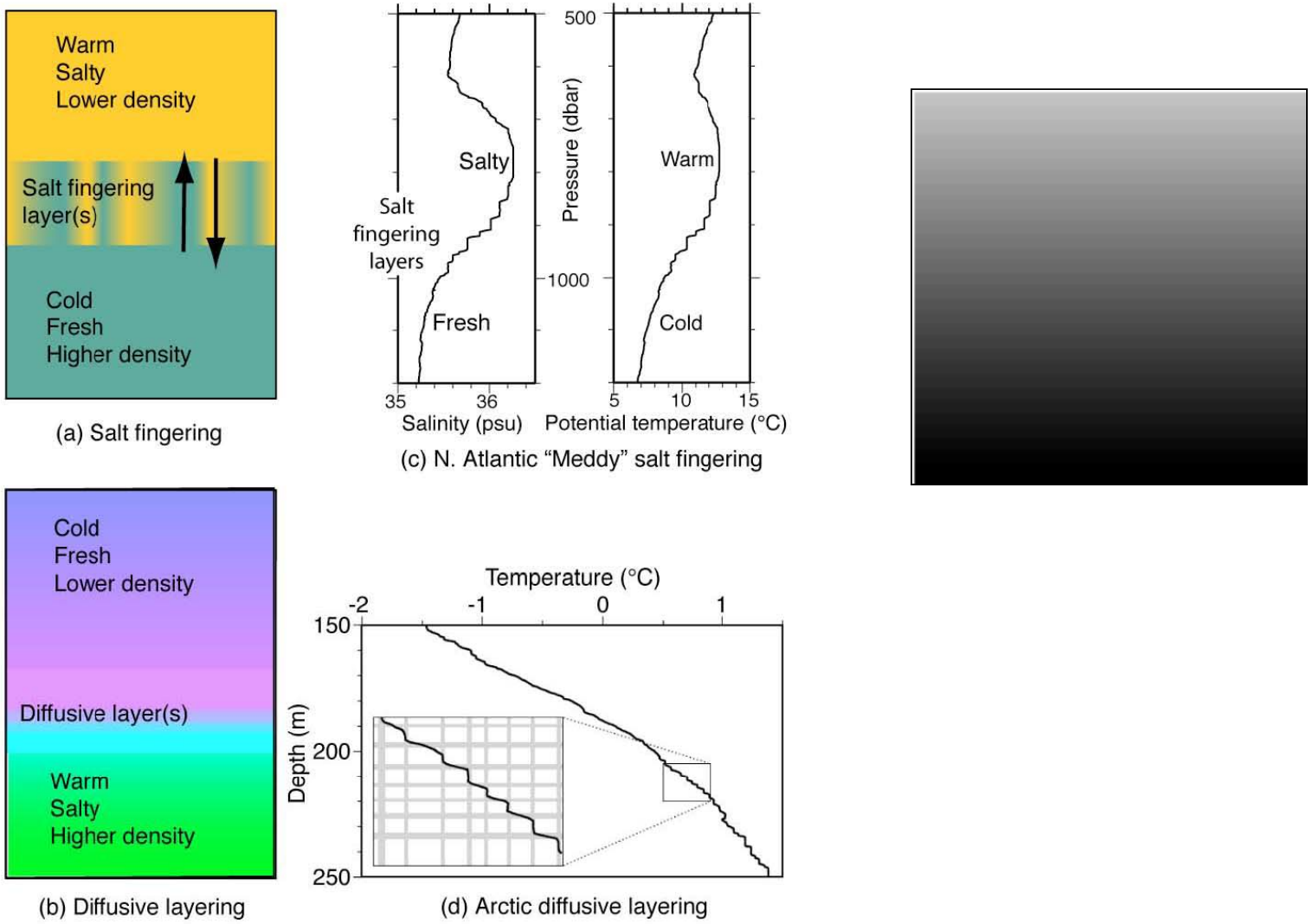

Fig. 8.8 Double diffusion: (a) Salt fingering interface (cold, fresh water warms and rises; warm, salty water cools and sinks). (b) Diffusive interface. (c) North Atlantic Mediterranean eddy salinity profile with steps due to salt fingering (25° 23'N, 26°W). (d) Arctic temperature profile with diffusive layering (Kelley et al. 2001).

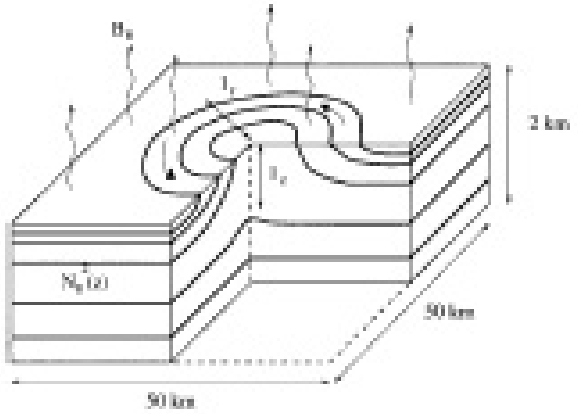

FIG. 1. A schematic diagram showing the simulation volume: an area 50 km × 50 km across and 2 km deep. Initially the whole domain is stably stratified, with a region of weaker stratification: a cold core eddy associated with a cyclonic shear. The eddy anomaly has a Gaussian form in the horizontal, decaying on a length scale L_r, and decays exponentially in the vertical over a scale L_z. The anomalous stratification in the center of the eddy is $N_0^2(z)$ where $N_0^2(z) < 0$; the background stratification is $N_1^2(z)$. A uniform surface buoyancy flux B_0 is applied over the whole domain.

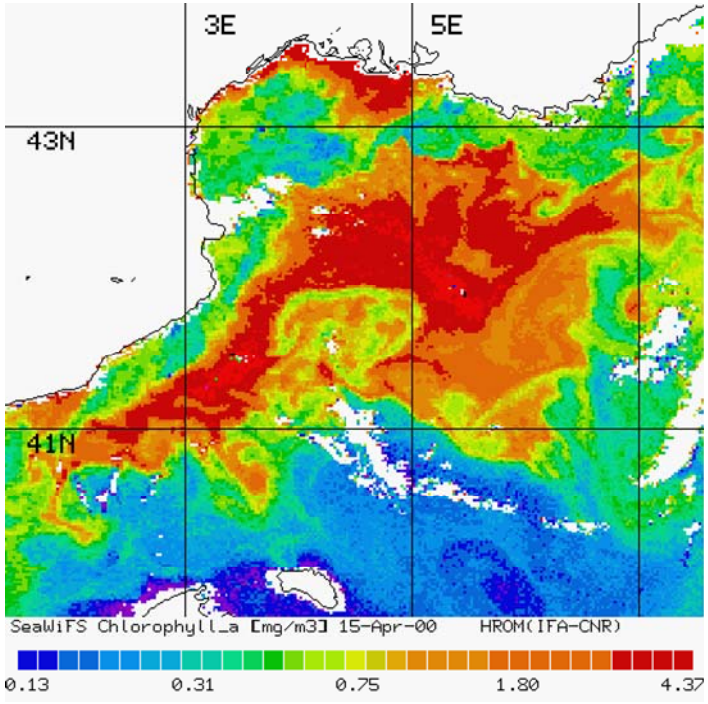

Different phase of the deep water simulation

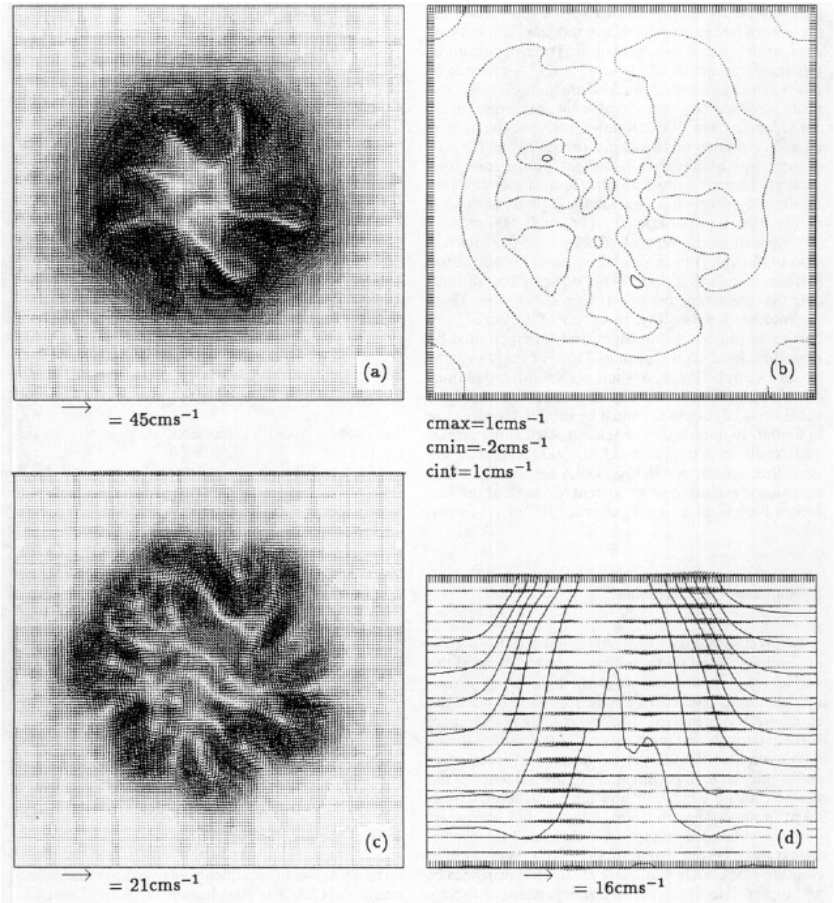

FIG. 20. The weakly stratified chimney simulation at day 3 with a format as in Fig. 14.

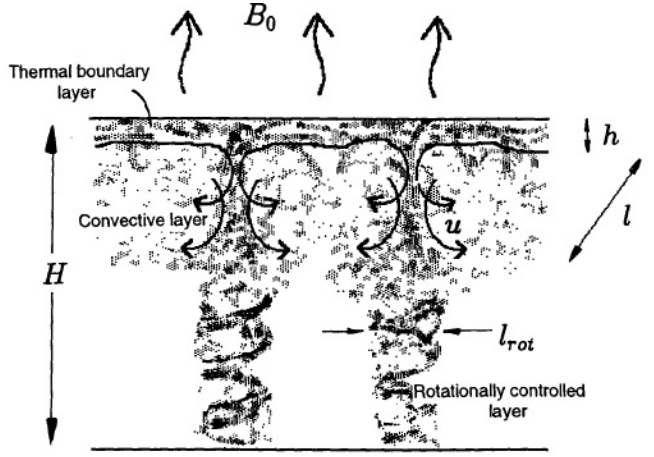

FIG. 1. A schematic representation of the "violent mixing" phase. A homogeneous ocean of depth H, exposed to surface negative buoyancy forcing B_0, responds through the development of a thermal boundary layer of depth h. From this layer intrusions of dense fluid—plumes—penetrate into the quiescent waters beneath having a characteristic length scale l and velocity scale u. These convective circulations sweep fluid out of the boundary layer to depth (and draw fluid up to the surface to be cooled) driving the convection layer below. If the ocean is sufficiently deep (as drawn here) then the convection layer will come under rotational control on the scale $l_{rot} = (B_0/f^3)^{1/2}$.

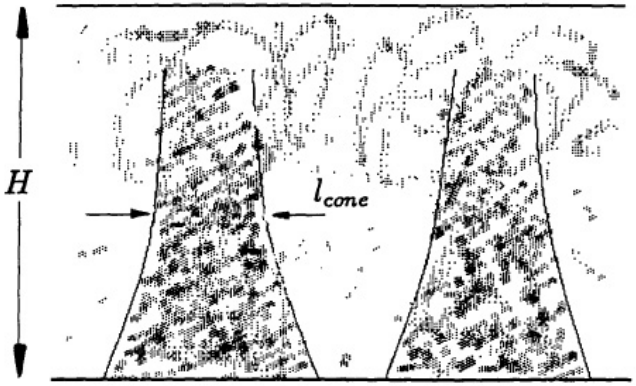

FIG. 2. A schematic representation of the earliest stages of the "sinking and spreading" phase. If $l_{rot} \ll H$, convectively modified waters, strongly under the influence of the earth's rotation, extend to the ocean bottom and "fill out" to the deformation radius l_e. "Cones" of spinning fluid are formed that trap the convected water and have a scale close to l_e.

- “deep mixing is not occuring by simple overturning of surface mixing layer, but rather through a complex hierarchy of mixing scales and dynamical processes” (Gascard, 1983)

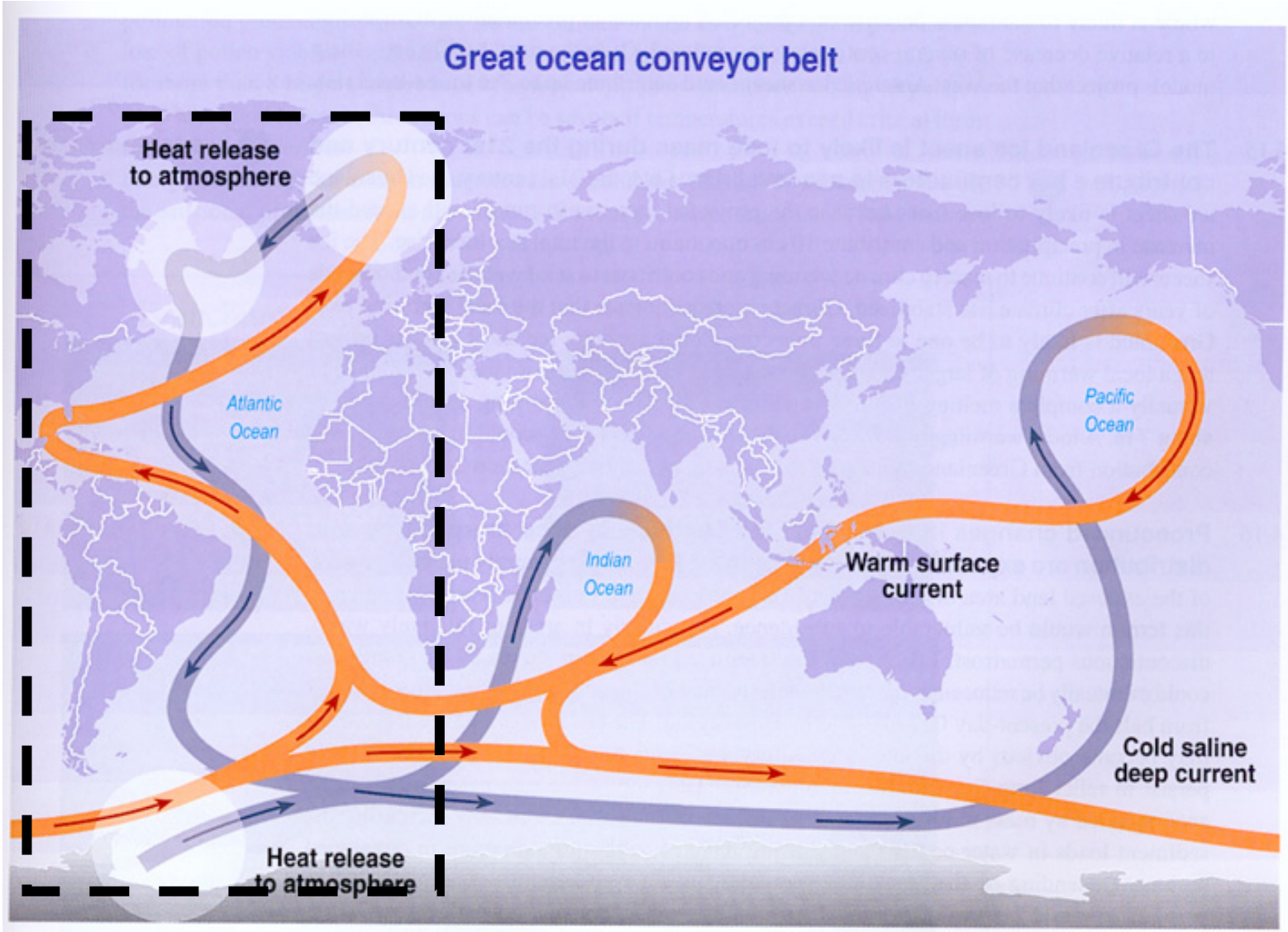
Great ocean conveyor belt
Heat release to atmosphere
Atlantic Ocean
Indian Ocean
Pacific Ocean
Warm surface current
Cold saline deep current
Heat release to atmosphere

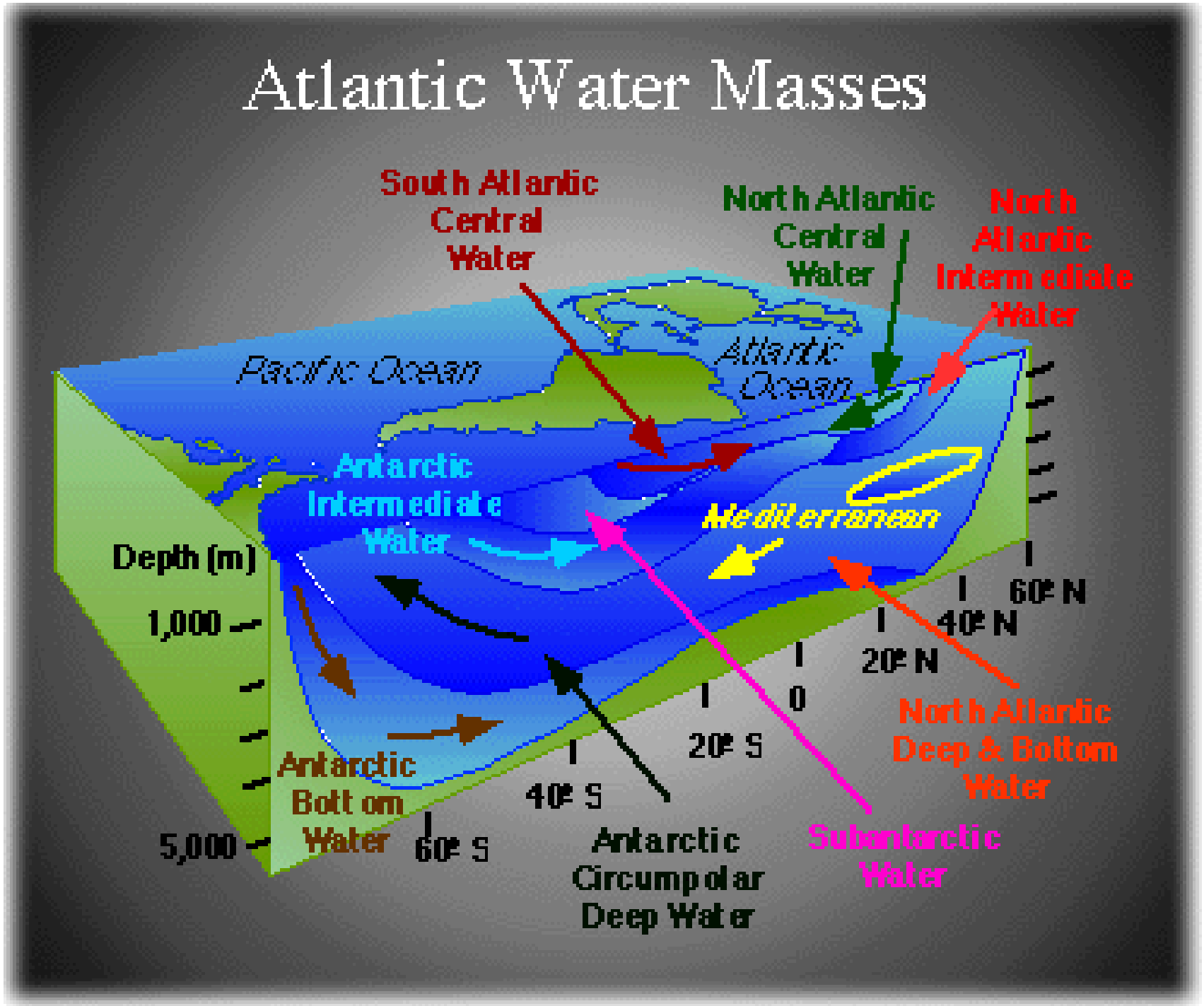
Atlantic Water Masses
South Atlantic Central Water
North Atlantic Central Water
North Atlantic Intermediate Water
Pacific Ocean
Atlantic Ocean
Antarctic Intermediate Water
Mediterranean
Depth (m)
1,000
5,000
60° S
40° S
20° S
0
20° N
40° N
60° N
Antarctic Bottom Water
Antarctic Circumpolar Deep Water
Subantarctic Water
North Atlantic Deep & Bottom Water

THE OCEAN CONVEYOR

carries warm surface waters from the tropics northward. At high latitudes, the waters cool, releasing heat to the atmosphere and moderating wintertime climate in the North Atlantic region. The colder (and denser) waters sink and flow southward in the deep ocean to keep the conveyor moving.

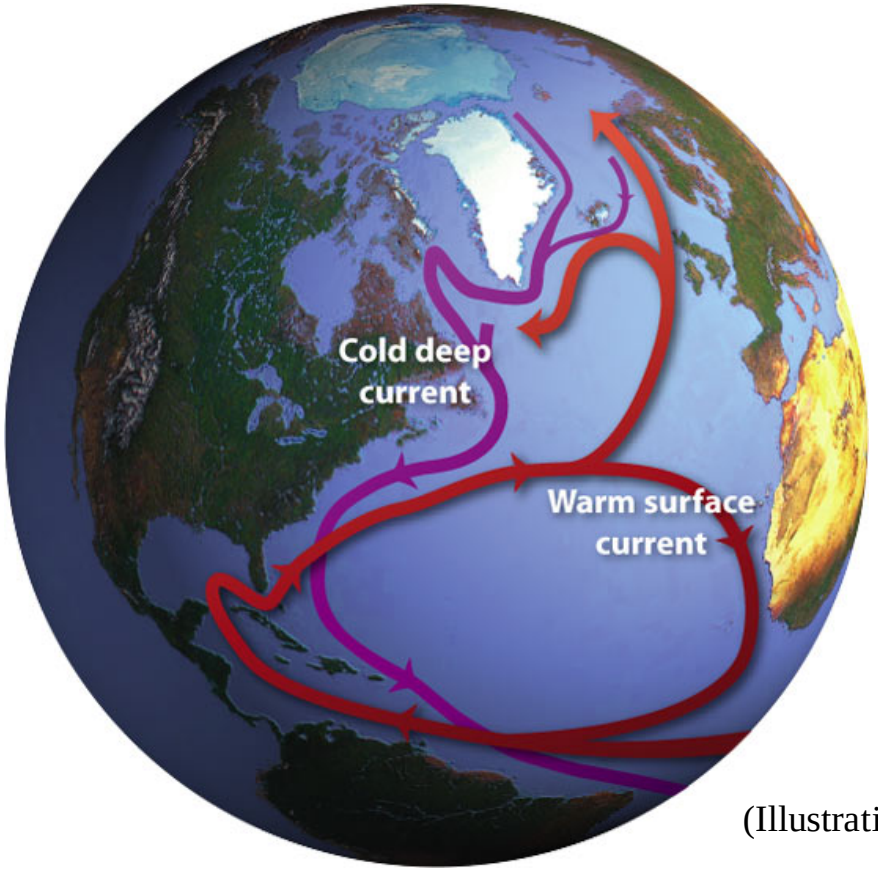

(Illustration by Jack Cook, WHOI)

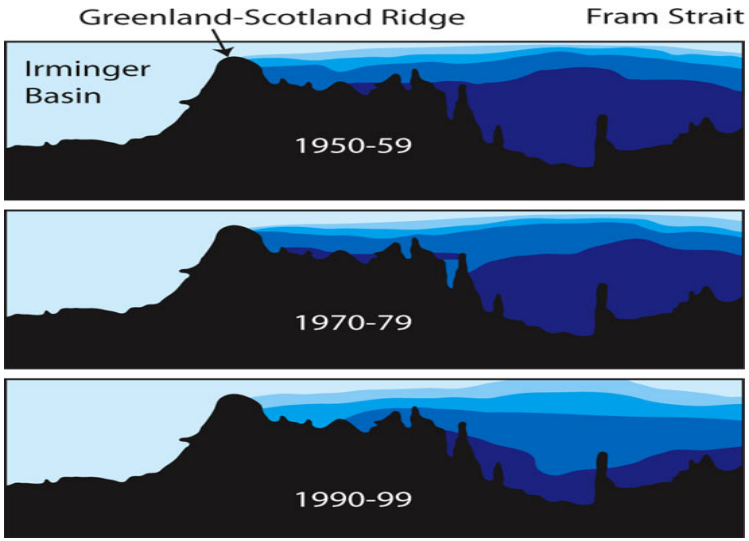
Greenland-Scotland Ridge
Fram Strait
Irminger Basin
1950-59
1970-79
1990-99

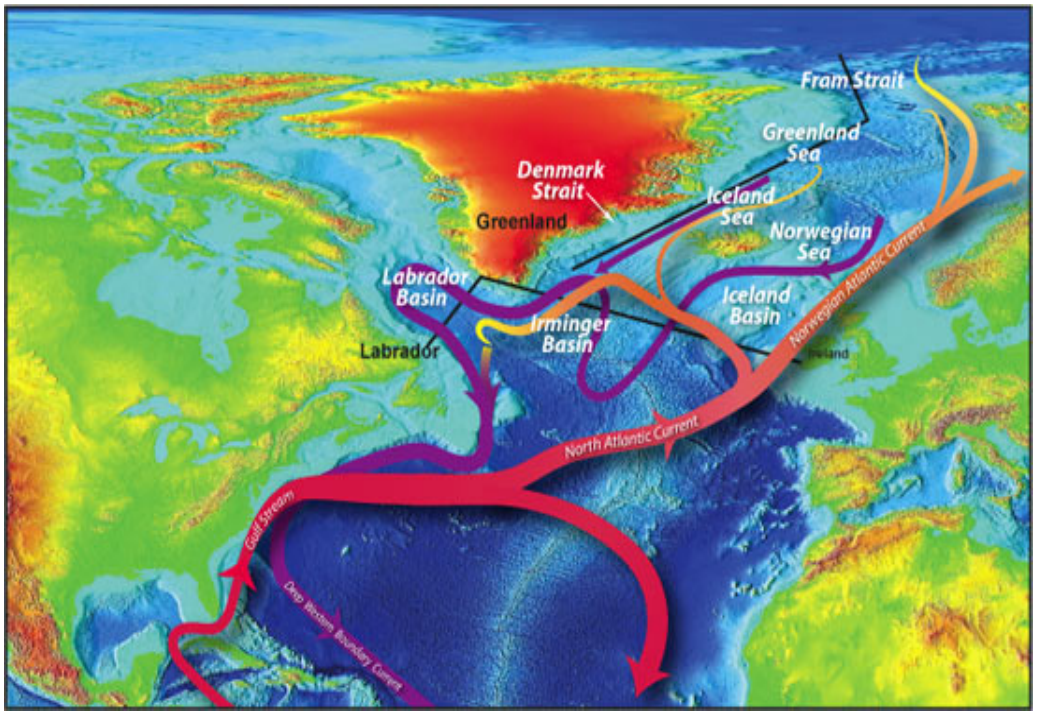
Fram Strait
Greenland Sea
Denmark Strait
Greenland
Iceland Sea
Norwegian Sea
Labrador Basin
Iceland Basin
Irminger Basin
Labrador
Norwegian Atlantic Current
North Atlantic Current
Gulf Stream
Deep Western Boundary Current

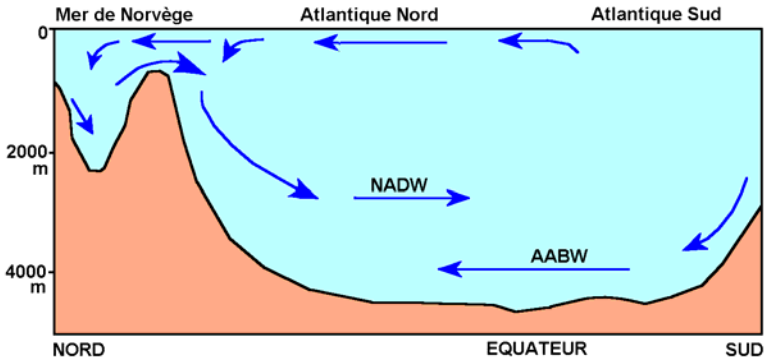
Mer de Norvège
Atlantique Nord
Atlantique Sud
0
2000 m
4000 m
NADW
AABW
NORD
EQUATEUR
SUD

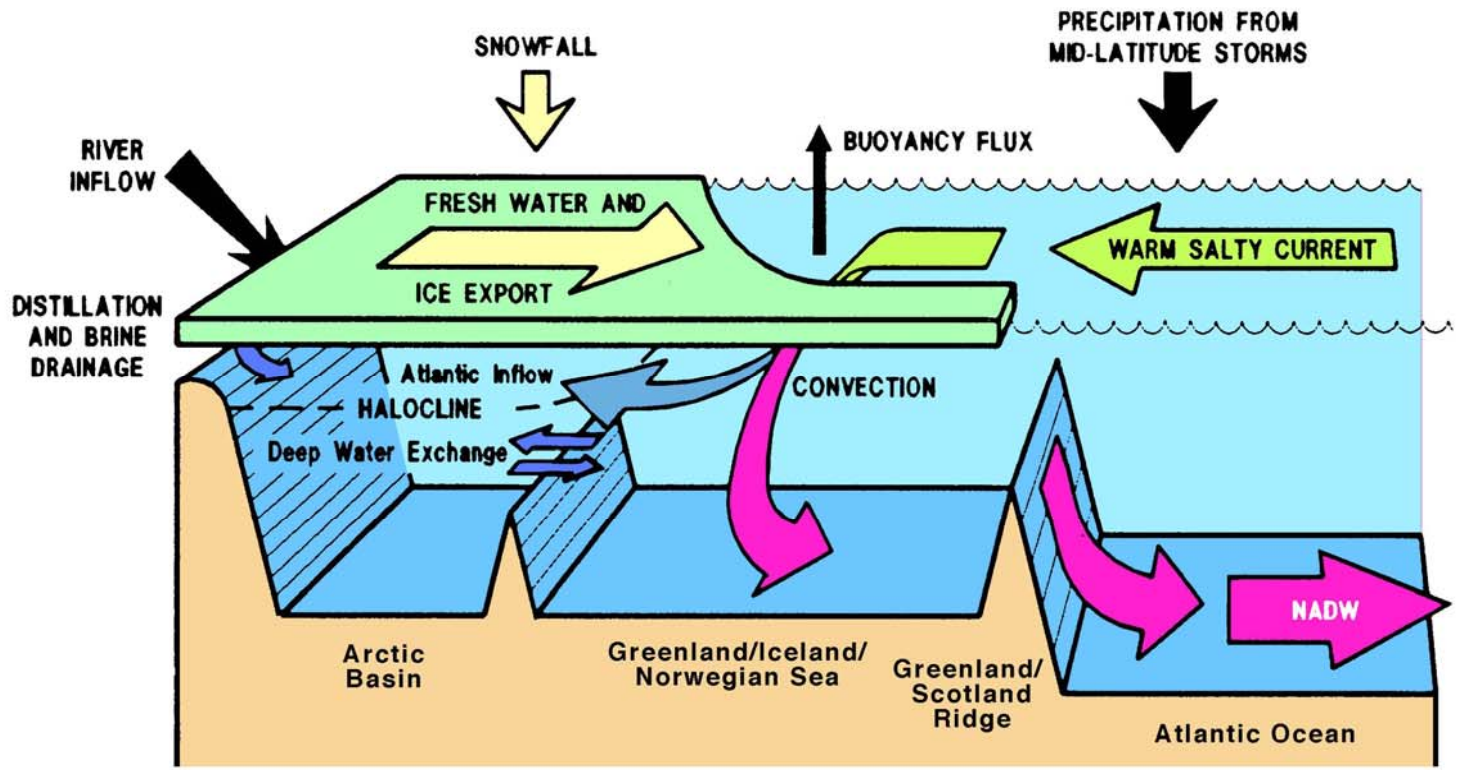

Fig. 20.13. Sketch of the circulation in the north Atlantic Ocean.

The stability of the ocean circulation

- Changes in ocean circulation can have an enormous effect on climate due to a strong modification of the pole ward heat transport
- There are evidences that rapid transition between warm and cold periods have occured
- Importance to understand the processes by which the global ocean circulation pattern can be changed
- Sensitivity study of the present ocean circulation under disturbances
- Keys area (Achille’s heel) that can respond rapidally to this external pertubation

A Thresholds

- Strongly discontinuous responses to projected climate change

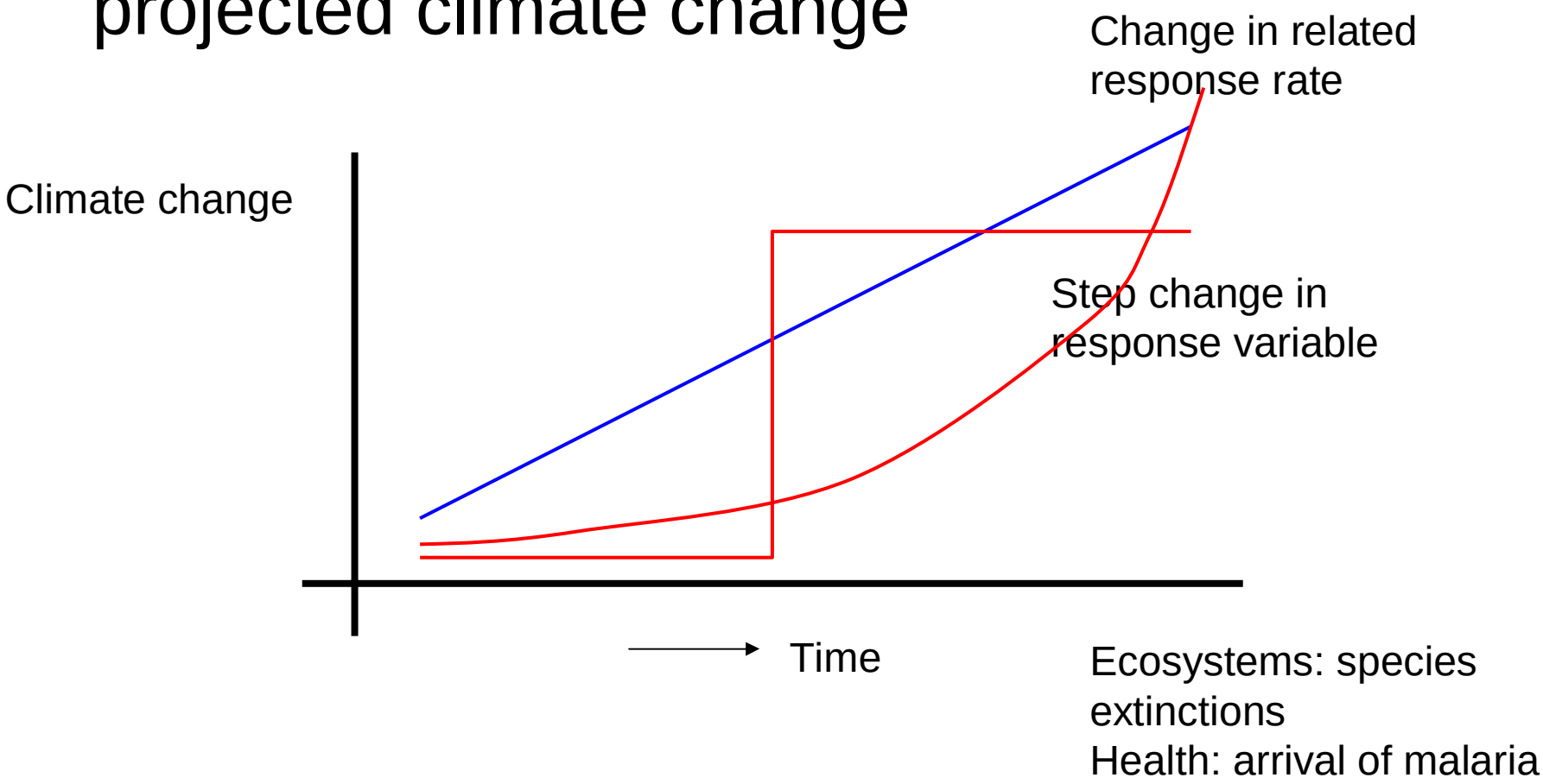

- The present atlantic circulation has 1-cell strutture with a northward surface flow and a conpensating southward deep sea circulation
- All the above considerations motivate studies of the thermohaline ocean circulation

- Stommel (1961) showed that the presence of heat and salt, with their different influence on the density field, may lead to steady stable regime (multiple steady state of ocean circulation)
- Bryan (1986) showed that perturbing the symmetric 2-cell state also 1-cell pole-to-pole asymmetric stable steady state may exist

- The transition is due to feedback processes induced by salinity anomaly at high latitude on the 2-cell state with equatorial upflow: an advective feedback processes between the strength of the circulation and the associated salt transport

- Box model may serve as a “toy” models to investigate one particular problem (like the influnze of the internal anomaly)
- Although these models are highly idealized as ocean model, the results obtained have shown many similarities with those of complex 3-D ocean models

circolazione termoalina

temperature change + temperature advection =
heating/cooling term + diffusion

salinity change + salinity advection =
evaporation/precipitation/brine
rejection + diffusion (8.42b)

For the mathematically-oriented reader, these equations are:

$$\partial T/\partial t + u\,\partial T/\partial x + v\,\partial T/\partial y + w\,\partial T/\partial z = Q_H/\rho c_p + \partial/\partial x(\kappa_H \partial T/\partial x) + \partial/\partial y(\kappa_H \partial T/\partial y) + \partial/\partial z(\kappa_V \partial T/\partial z) \quad (8.43a)$$

$$\partial S/\partial t + u\,\partial S/\partial x + v\,\partial S/\partial y + w\,\partial S/\partial z = Q_S + \partial/\partial x(\kappa_H \partial S/\partial x) + \partial/\partial y(\kappa_H \partial S/\partial y) + \partial/\partial z(\kappa_V \partial S/\partial z) \quad (8.43b)$$

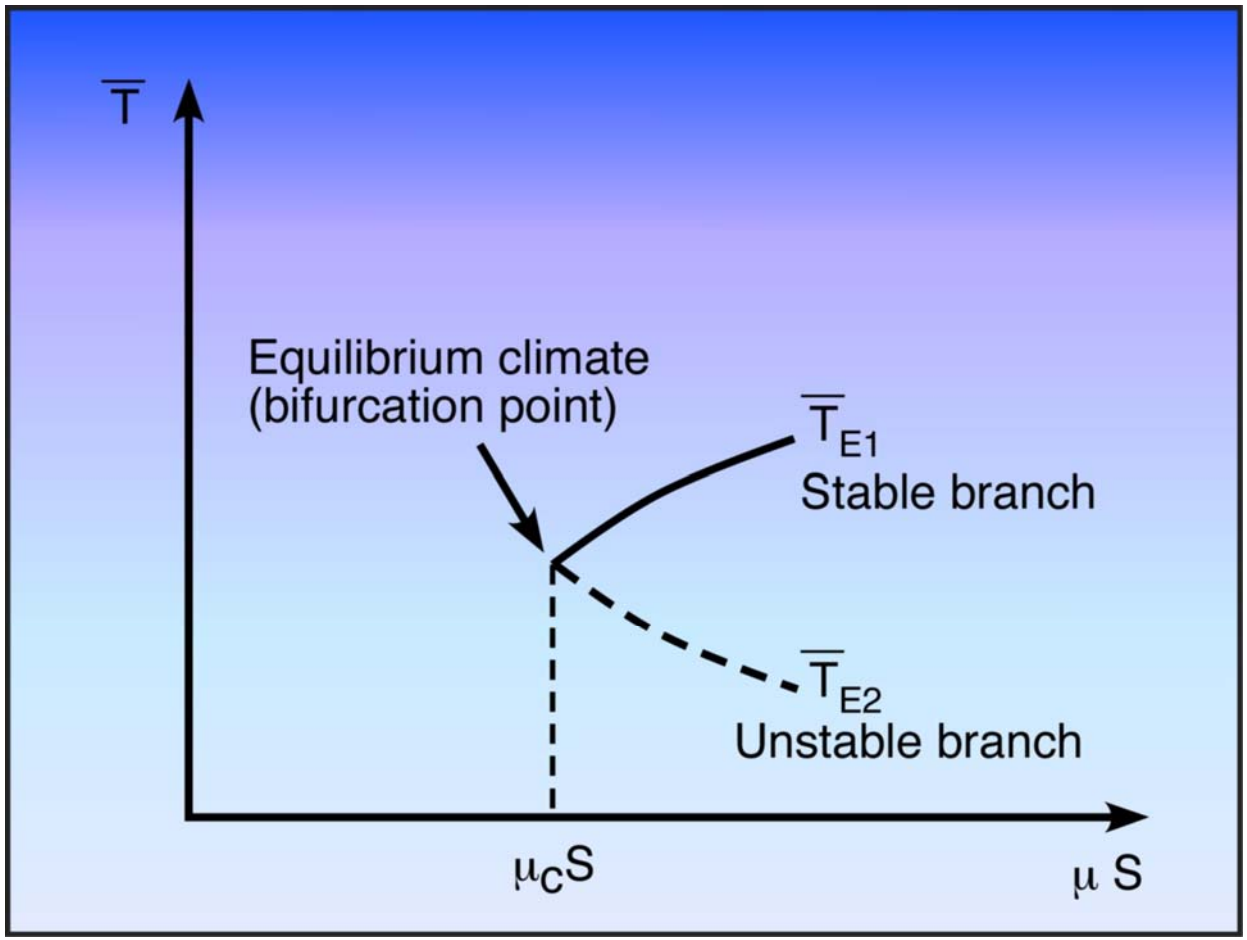
$\overline{T}$
Equilibrium climate
(bifurcation point)
$\overline{T}_{E1}$
Stable branch
$\overline{T}_{E2}$
Unstable branch
$\mu_c S$
μ S

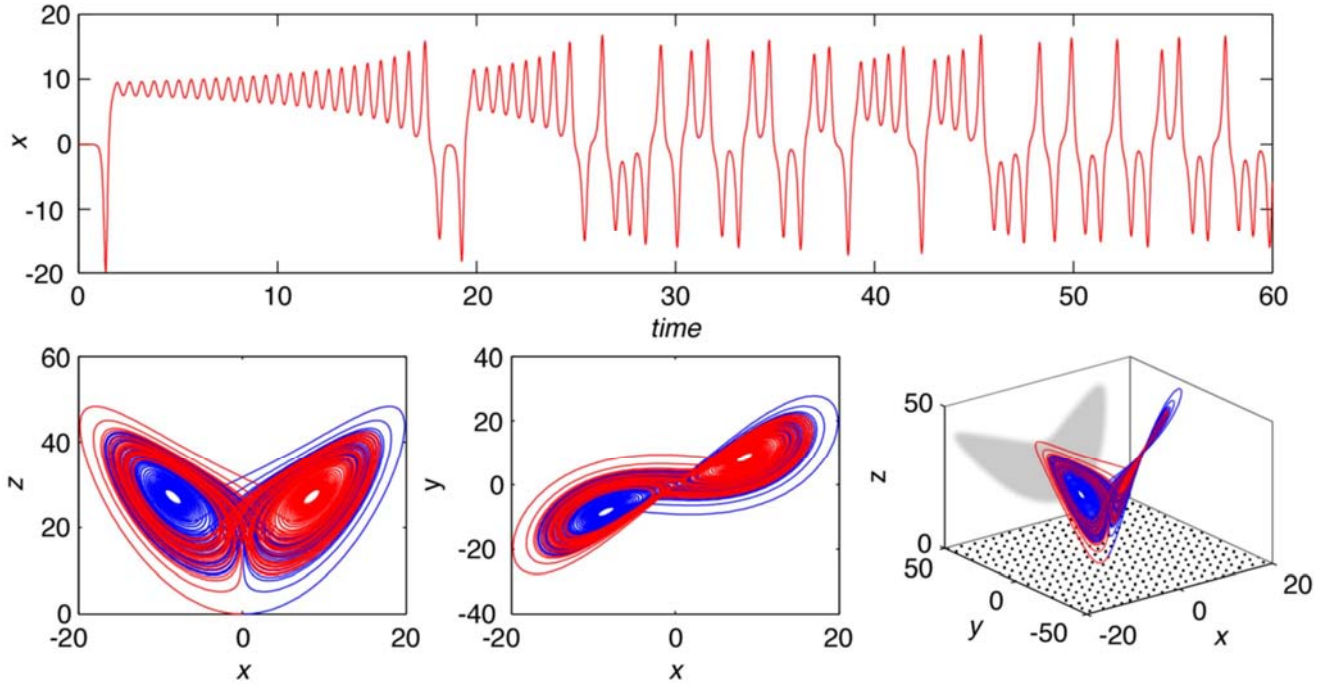
20
10
0
-10
-20
x
0
10
20
30
40
50
60
time
60
40
20
0
z
-20
0
20
x
40
20
0
-20
-40
y
-20
0
20
x
50
0
z
50
0
y
-50
-20
0
20
x

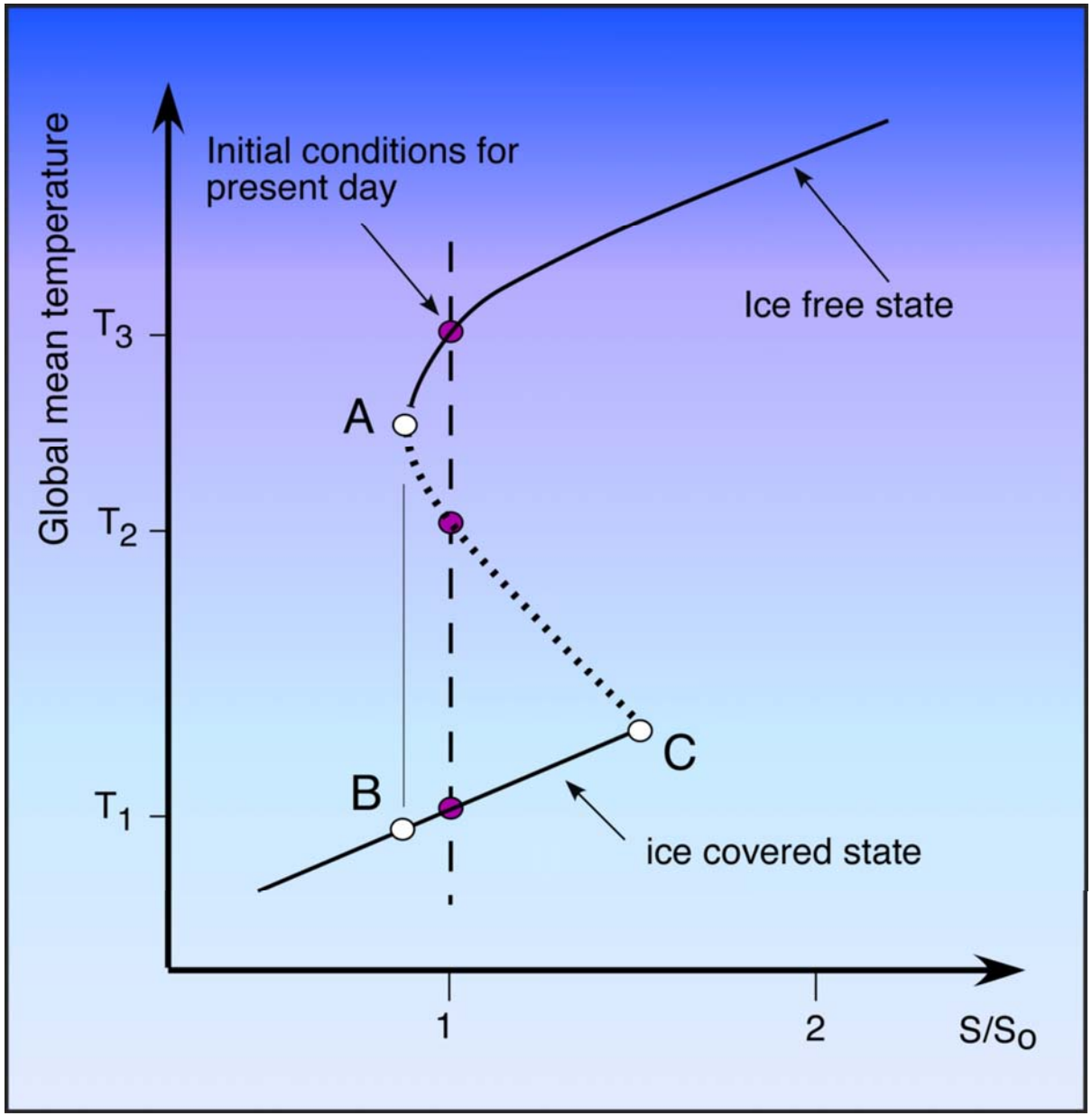
Global mean temperature
Initial conditions for present day
Ice free state
A
B
C
ice covered state
T_3
T_2
T_1
1
2
S/S_o

MULTIPLE EQUILIBRIA OF THC

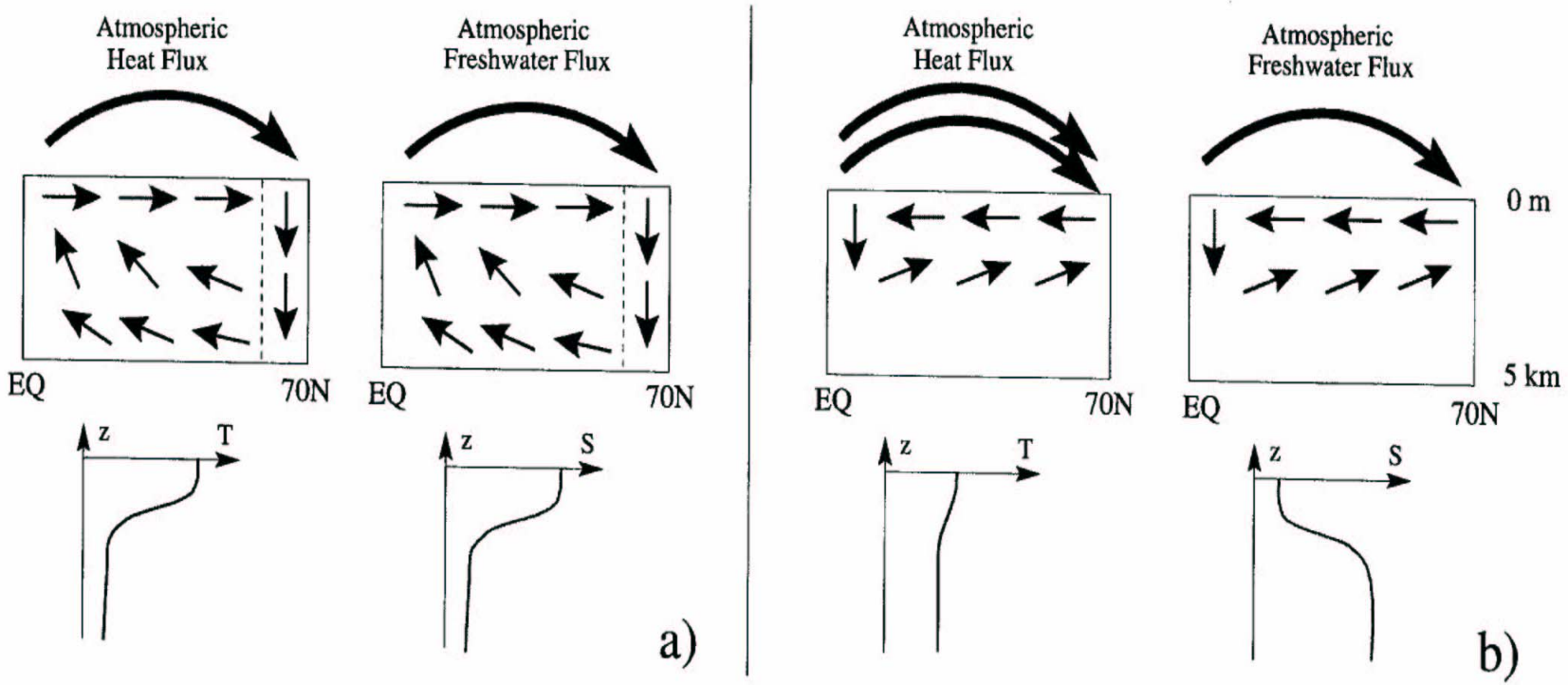

Fig. 3. Schematic representation of the basic mechanisms responsible for multiple equilibria of the THC in a simple hemispheric configuration (top row) and typical vertical profiles of temperature and salinity in the high latitudes (bottom row) for the corresponding circulation types. (a) Direct circulation. (b) Indirect circulation.

Table 1
Summary of the two principle feedback mechanisms that cause changes of the thermohaline circulation. The table is an extended version of Rahmstorf (1998); further feedback mechanisms are discussed in Marotzke (1996).

	ADVECTIVE FEEDBACK	CONVECTIVE FEEDBACK
Process	Advection of high salinity waters from the evaporative regions of the low latitudes to the deep water formation regions	Localized, upward mixing of warmer and more saline water into the surface layers of the high latitudes where cooling and excess precipitation prevails
Time scale	10–100 yr	1–10 yr
Trigger	Large-scale perturbation of atmosphere-ocean heat and freshwater fluxes, reduction of deep water formation at high latitudes	Localized input of freshwater, changes of sea ice cover, local changes in atmosphere-ocean heat and freshwater fluxes
Representation in models	Large-scale, robust process, fairly well represented in box models to coupled atmosphere-ocean general circulation models	Poorly parameterized in all coarse-resolution models. Only non-hydrostatic, high-resolution models simulate this process

6.1 LOCAL (OR INTERNAL) STABILITY

For generality, let us consider the stability properties of any equilibrium (steady state) of a system of equations of the form

$$\frac{dx_i}{dt} = f(x_i) \tag{6.1}$$

where x_i denotes a set of variables. Small departures, x_i', from a steady-state $x_{i(0)}$ satisfying $f(x_{i0}) = 0$ are governed by the linearized form of Eq. (6.1),

$$\frac{dx_i'}{dt} = J_0 x_i' \tag{6.2}$$

where J_0 is the Jacobian matrix, $(\partial f/\partial x_j)_0$, evaluated at $x_i^{(0)}$. Then assuming departures of the form $x' \sim \exp(\omega t)$, where ω are the eigenvalues, the local behavior near $x_{i(0)}$ is determined by the roots of the equation

$$\text{Determinant}\{\omega\delta_{ij} - J_0\} = 0 \tag{6.3}$$

where δ_{ij} is the Kronecker delta. If all the eigenvalues have negative real parts the steady state is stable, and if one or more eigenvalues has a positive real part then the steady state is unstable.

6.3 STRUCTURAL (OR EXTERNAL) STABILITY: ELEMENTS OF BIFURCATION THEORY

In Section 6.1 we discussed the stability of a particular equilibrium point in a system when an internal state variable is perturbed from this point, holding all external factors fixed. We now consider the changes in the number, values, and internal stability of all the equilibria of a system when an external factor (i.e., a control variable) is changed. The stability of the equilibrium structure in the face of changes in a control variable has variously been called *global* (as opposed to *local*), external, or structural stability. The critical values of the control parameters at which discontinuous changes in the equilibrium structure occur are called bifurcation points.

To illustrate we first consider the properties of the single-variable equation, Eq. (6.11), reduced to its symmetric cubic form ($k_2 = 0$),

$$\frac{dz}{dt} = cz - k_3 z^3 \tag{6.12}$$

which can be rewritten in a normal form by scaling $z = k_3^{-1/2} Z$, i.e.,

$$\frac{dZ}{dt} = cZ - Z^3 \tag{6.13}$$

This equation has three equilibria Z_0 (fixed points) for $c > 0$: $Z_0^{(0)} = 0$, $Z_0^{(1)} = c^{1/2}$, and $Z_0^{(2)} = -c^{1/2}$. These equilibria are graphed as a function of c in Fig. 6-1, which is the *bifurcation diagram* for Eq. (6.13), revealing its structural stability properties, including the "pitchfork" bifurcation at $c = 0$. At this bifurcation point the equilibrium $Z = 0$ which is stable for all $c < 0$, becomes unstable for all $c > 0$, a symmetric pair of stable equilibria emerging parabolically with increasing c. As is conventional, solid curves denote locally stable equilibria and dashed curves denote locally unstable equilibria.

In Fig. 6-2 we plot (a) $\dot{Z}$ as a function of Z and (b) the Lyapunov potential implied by Eq. (6.13), defined by $V_Z = -\int [cZ + Z^3]\, dZ$, showing the generic property of the cubic form in confining an unstable equilibrium ($Z_0^{(0)}$) between two stable equilibria $Z_0^{(1)}$ and $Z_0^{(2)}$. This common physical situation will appear in relation to the EBM

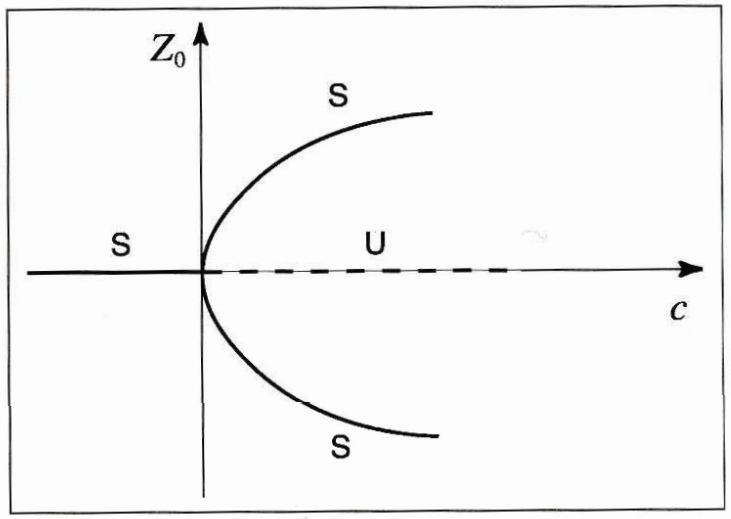

Figure 6-1 Bifurcation diagram for Eq. (6.13). Stable and unstable equilibrium branches denoted by S and U (dashed), respectively.

to be discussed in Chapter 7 and the simple two-box ocean model to be discussed in Chapter 11.

Although the pitchfork bifurcation just described provides the most elemental, physically significant representation of an unstable system, for completeness we mention two other basic "normal forms" and their bifurcation diagrams.

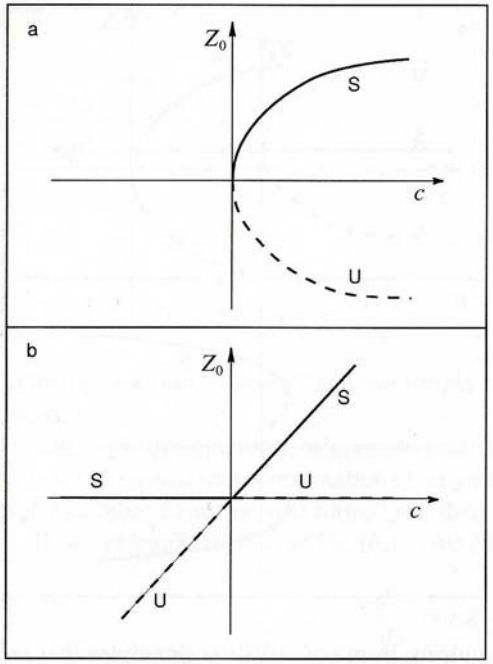

Figure 6-5 Bifurcation diagram for Eq. (6.16) illustrating a saddle node (*or limit point*) bifurcation (a), and for Eq. (6.17), illustrating a *transcritical* bifurcation (b).

Other possibilities are represented by normal forms for a single variable in which damping occurs at the quadratic rather than cubic level. These include the form

$$\frac{dZ}{dt} = c - Z^2 \tag{6.16}$$

which gives rise to the *saddle node* (or *limit point*) bifurcation shown in Fig. 6-5a, and the form

$$\frac{dZ}{dt} = cZ - Z^2 \tag{6.17}$$

which gives rise to the *transcritical bifurcation* diagram pictured in Fig. 6-5b. Note that in both cases transient departures from the equilibria will run away catastrophically from the lower unstable equilibrium, underlining the reasons why a cubic of the form given by Eq. (6.13) or (6.15) is the natural representation of the damping rate when a destabilizing first-order process is operative (i.e., $c > 0$).

To conclude our brief review of bifurcation properties for single-variable systems we consider what is called an "imperfect" form of Eq. (6.13) in which an external forcing function F is added, i.e.,

$$\frac{dZ}{dt} = cZ - Z^3 + F \tag{6.18}$$

In Fig. 6-6 we show the dependence of the equilibria on each of the two control variables F and c. The dependence on F takes the form of an S-shaped curve with two stable branches and one unstable branch. A periodic variation of F near the unstable branch can lead to a hysteresis loop, as shown by the arrows in Fig. 6-6a. This generic S-shaped equilibrium pattern is of the same form as the equilibrium patterns to be shown in Fig. 7-3 for the EBM and Fig. 11-5 for the Stommel two-box ocean model. In Fig. 6-6b we show the same equilibria as a function of c, holding F constant, in which case the equilibria no longer take the pure pitchfork form shown by the dotted curve; instead they are broken into two curves, one of which has an unstable branch, giving the appearance of an imperfect pitchfork.

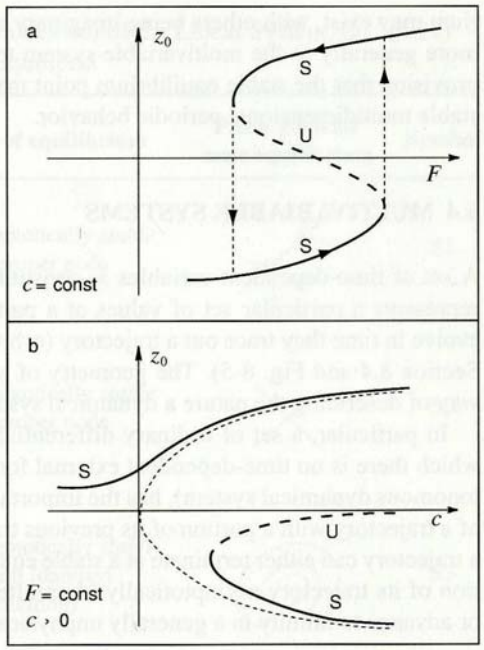

Figure 6-6 Bifurcation diagram for Eq. (6.18) (a) as a function of F with c taken as a constant and (b) as a function of c with F taken as a nonzero constant.

THE A-O SYSTEM CAN EXHIBIT HYSTERESIS BEHAVIOUR (FROM STOKER, QSR, 2000)

LINEAR BEHAVIOUR

NON-LINEAR BEHAVIOUR
REVERSIBLE/IRREVERSIBLE
RESPONSE TO PERTURBATION

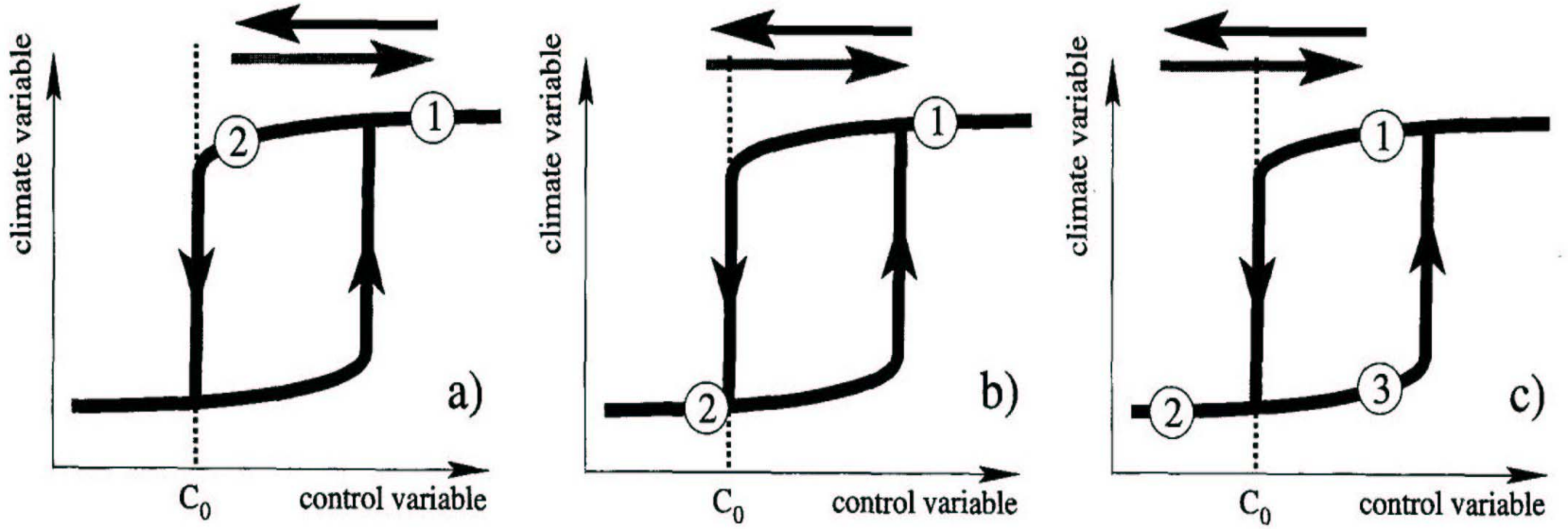

CRITICAL THRESHOLD OF THE CONTROL VARIABLE

LA RISPOSTA DEL SISTEMA CLIMATICO AI FORZANTI ESTERNI (E.G. SCIOGLIMENTO DEI GHIACCIAI) HA UN COMPORTAMENTO NON-LINEARE TIPO *ISTERESI (ovvero un giro sulle montagne russe)* OSSIA PER VALORI CRITICI DEI FORZANTI IL SISTEMA CROLLA PER POI RECUPERARE PER UN PERCORSO DIVERSO DA QUELLO PRECEDENTE

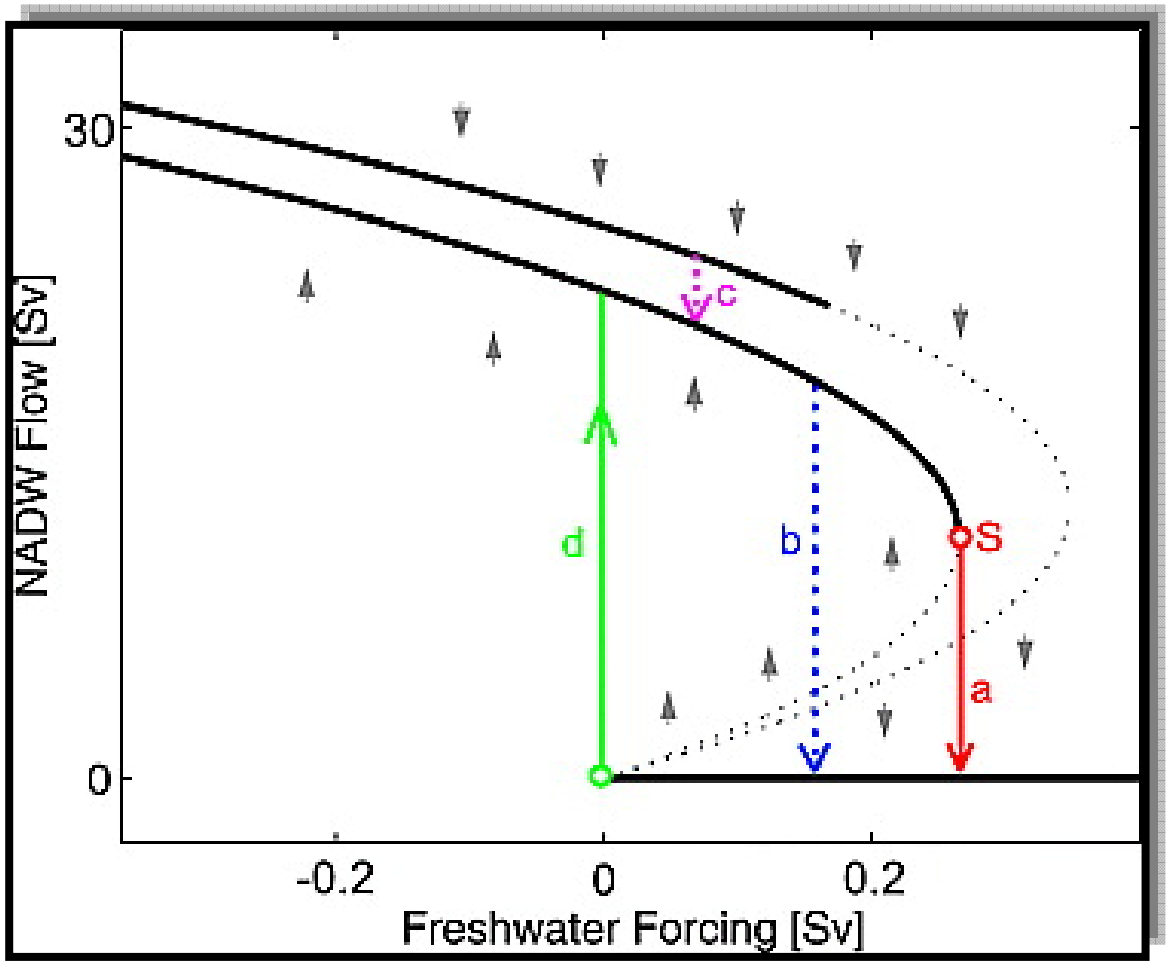

11.4.1 The Two-Box System

In a significant paper Stommel (1961) showed how the difference in the contributions of temperature and salinity to this pole to equator density difference can give rise to an instability in the ocean that can result in multiple equilibrium states. Stommel's result was based on a two-box simplification of the four-box model described in Section 11.2 in which boxes 1 and 4, and boxes 2 and 3, are each combined to form single low- and high-latitude boxes extending from the top to the bottom of the ocean, separated from each other at a distance $y = L$ from the equator $y = 0$.

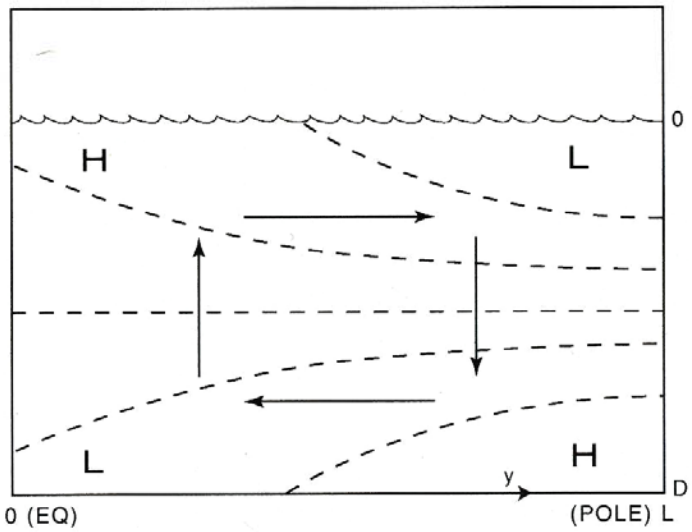

Figure 11-3 Schematic cross-section of the thermohaline circulation driven by pressure differences engendered hydrostatically by equator-to-pole density variations.

Here we shall start by considering a more detailed three-box version of Fig. 11-1 in which we retain a representation of the relatively faster response upper layer ($\Delta Z = d$), wherein the gradients of T and S forced by surface fluxes of heat and freshwater are a maximum; these fluxes can be approximated by distinct well-mixed values in each of boxes 1 and 2. The region below this upper level ($\Delta Z = D - d$) is represented by a single well-mixed deep ocean layer formed by combining boxes 3 and 4 of Fig. 11-1 (cf. Birchfield *et al.*, 1990). The properties of this large volume of deep ocean vary on a longer time scale in response to small net fluxes of heat and salt across $Z = d$. We designate the value of temperature and salinity in this deep ocean by θ and S_D, respectively. To reduce this three-box ocean to a Stommel-like two-box ocean we can define a high-latitude (polar) state

$$(T_p, S_p) \equiv \frac{(T_1, S_1)V_1 + (\theta, S_D)V_4}{V_p} \tag{11.18}$$

and a low-latitude (equatorward) state

$$(T_e, S_e) \equiv \frac{(T_2, S_2)V_2 + (\theta, S_D)V_3}{V_e}$$

where $V_p \equiv (V_1 + V_4)$ and $V_e \equiv (V_2 + V_3)$. Because heat and freshwater fluxes occur at the ocean surface it is reasonable to assume that most of the poleward change in T and S occurs mainly between the upper boxes (1 and 2), with relatively uniform values in the combined deep water box (3 and 4).

Averaging Eqs. (11.4) and (11.5) over the climatic-average period $\delta_c = 100$ y (thereby excluding explicit consideration of all subcentennial scale variability, including interdecadal variability), averaging spatially over each of the two volumes V_p and V_e, and applying the boundary conditions $w = 0$ at the surface ($Z = 0$) and bottom ($Z = D$) and $v = 0$ at the equator ($y = 0$) pole ($y = L$), we obtain the following set of equations governing the mean values of T and S in each volume (see Fig. 11-4).

$$V_p \frac{dT_p}{dt} = Q_T + \mathcal{H}_p^{\uparrow} + \mathcal{G}_p^{\uparrow} \tag{11.19a}$$

$$V_e \frac{dT_e}{dt} = -Q_T - \mathcal{H}_e^{\downarrow} + \mathcal{G}_e^{\uparrow} \tag{11.19b}$$

$$V_p \frac{dS_p}{dt} = Q_s - \mathcal{F}^{\downarrow} S_p \tag{11.20a}$$

$$V_e \frac{dS_e}{dt} = -Q_s + \mathcal{F}^{\uparrow} S_e \tag{11.20b}$$

where the well-mixed climatic-mean values of T and S in each box, n, are

$$(T_n, S_n) = \frac{1}{V_n} \iiint_n (T, S)\, dx\, dy\, dz. \tag{11.21}$$

Recalling our definitions [Eqs. (7.2) and (7.3)] of the zonal average $\langle x \rangle \equiv W^{-1} \int x\, dx$ (where in this case W is the width of an ocean basin) and of the departure representing mean gyres is $x_* \equiv x - \langle x \rangle$, the net thermal and salinity fluxes across a latitude wall at $y = L^*$ are

$$\begin{aligned} Q_{(T,S)} &= \int_0^D \int_0^W \left\langle \overline{v \cdot (T, S)} \right\rangle_{L^*} dx\, dz \\ &= Q_{(T,S)\psi} + Q_{(T,S)\phi} + Q^{\star}_{(T,S)} \end{aligned} \tag{11.22}$$

where $Q_{(T,S)\psi} = \iint \langle v \rangle \langle (T, S) \rangle\, dx\, dz$, $Q_{(T,S)\phi} = \iint \langle v_* (T, S)_* \rangle\, dx\, dz$, and $Q^{\star}_{(T,S)} = \iint \langle \overline{v^{\star} \cdot (T, S)^{\star}} \rangle\, dx\, dz$ are the respective contributions due to the mean thermohaline circulation $\langle v \rangle$, mean gyre flow $v_* = (\partial \phi / \partial x)$, and subclimatic-mean circulations $v^{\star}$, including phenomena such as baroclinic eddies and interdecadal fluctuations [see Eq. (5.3)].

The upward fluxes of sensible heat at the ocean surface $\mathcal{H}_n^{\uparrow}$, the geothermal flux at the bottom $\mathcal{G}^{\uparrow}$ (both in units of $\mathrm{m^3\,K\,s^{-1}}$) and the freshwater flux $\mathcal{F}_n^{\uparrow}$ (in units of $\mathrm{m^3\,s^{-1}}$), across the horizontal area A_n of each region, are

$$\left(\mathcal{H}_n^{\uparrow}, \mathcal{G}_n^{\uparrow}, \mathcal{F}_n^{\uparrow}\right) = \iint_{A_n} \left[\left(H_{\mathrm{SS}}^{\uparrow}/\rho c\right), \left(H_{\mathrm{D}}^{\uparrow}/\rho c\right), \left(F^{\uparrow}/\rho\right)\right] dx\, dy \tag{11.23}$$

Note that Eqs. (11.20a) and (11.20b) imply conservation of salt for the whole ocean (the validity of which over geologic time can only be assumed), but not of global mean salinity,

$$\breve{S} = \frac{V_{\mathrm{e}} S_{\mathrm{e}} + V_{\mathrm{p}} S_{\mathrm{p}}}{V} \tag{11.24}$$

which can be expected to vary as a consequence of changing storage in the cryosphere (i.e., $\mathcal{F}_{\mathrm{e}}^{\uparrow} \neq \mathcal{F}_{\mathrm{p}}^{\downarrow}$). That is,

$$\frac{d\Pi_{\mathrm{salt}}}{dt} = 0 \tag{11.25}$$

where $\Pi_{\mathrm{salt}} = \rho^*(V_{\mathrm{p}} S_{\mathrm{p}} + V_{\mathrm{e}} S_{\mathrm{e}})$ and ρ^* is the standard seawater density. To demonstrate consistency with Eqs. (11.20a) and (11.20b), note that $\mathcal{F}_{\mathrm{e}}^{\uparrow} = -dV_{\mathrm{e}}/dt$ and $\mathcal{F}_{\mathrm{p}}^{\downarrow} = dV_{\mathrm{p}}/dt$.

If one assumed no net mean temperature change of the whole ocean, then $\mathcal{H}_{\mathrm{p}}^{\uparrow} = \mathcal{H}_{\mathrm{e}}^{\downarrow}$. As in the case of the freshwater balance on paleoclimatic time scales, however, we can expect small imbalances in the net surface heat flux that ultimately lead to slow variations in the mean temperature of the deep ocean (see Section 8.3). In general, $\mathcal{H}^{\uparrow}$ is a fast-response surficial variable, calculable from a GCM as a function of prescribed slow-response variables, i.e., $\mathcal{H}^{\uparrow} = \mathcal{H}^{\uparrow}(I, \mu, \theta)$.

In many studies $\mathcal{H}^{\uparrow}$ has been represented by a Newtonian approximation, the so-called "restoring condition" (Haney, 1971), i.e.,

$$\mathcal{H}_n^{\uparrow} = \Gamma\left(T_n - T_n^*\right) \tag{11.26}$$

where the vorticity is

$$\nabla^2\psi = \left(\frac{\partial v}{\partial z} - \frac{\partial w}{\partial y}\right) = -\left(\frac{\partial^2\psi}{\partial y^2} + \frac{\partial^2\psi}{\partial z^2}\right)$$

The Coriolis term $(-f\,\partial u/\partial z)$ is probably small compared to the density gradient and viscous terms, and is generally neglected (e.g., Cessi and Young, 1992) or is considered to be absorbed into the viscous terms (Sakai and Peltier, 1995); we shall neglect it here.

A solution satisfying the condition that the normal velocity on the boundaries vanishes (i.e., $\psi = 0$ on the boundaries) is of the form

$$\psi = \psi_{\max} \sin\frac{\pi}{L}\, y \cdot \sin\frac{\pi}{D}\, z \tag{11.33}$$

where $\psi_{\max}$ is the maximum value of ψ at $(L/2, D/2)$, measuring the strength of the TH circulation. This form represents a more symmetric overturning than pictured in Figs. 11-1 and 11-4, being similar to the idealized picture shown in Fig. 11-3. The governing equation for the variations of $\psi_{\max}$ is obtained by substituting Eq. (11.33) in Eq. (11.32), and integrating over the spatial domain $y = 0$ to L and $z = 0$ to D, yielding

$$\frac{d\psi_{\max}}{dt} = \frac{a}{\rho^*}\,(\rho_{\mathrm{p}} - \rho_{\mathrm{e}}) - \kappa\psi_{\max} \tag{11.34}$$

where $\rho_{\mathrm{p}} \equiv \rho(L)$, $\rho_{\mathrm{e}} \equiv \rho(O)$, and $a = [gLD^2/4(L^2 + D^2)]$, a constant.

Thus, the variations of $\psi_{\max}$ are driven by the density difference between the two volumes, under the retarding influence of linear dissipation. It is typically assumed that the viscous resistance represented by κ is large enough that a quasi-static equilibrium prevails $[d(\psi_{\max})/dt \approx 0]$ of the form

$$(\psi_{\max})_0 \approx -\frac{k_\psi}{\rho^*}\,\delta\rho \tag{11.35}$$

where $\delta\rho \equiv (\rho_{\mathrm{e}} - \rho_{\mathrm{p}})$, $k_\psi = a/\kappa$, and $\rho = \rho(T, S)$ in accordance with Eq. (11.6). Note that this assumption tends to place the circulation ψ in the category of a relatively "fast-response" variable (in comparison, e.g., with the deep ocean temperature θ; see Section 8.3), adjusting on a short time scale to an imposed density difference. On the other hand, because salinity has no intrinsic self-regulating dissipative property, it can fall in the category of a slow-response variable, especially if positive feedbacks occur, as will be discussed in more detail in Section 11.4.4. The other slower response variables that ultimately control the variations of the density difference include the deep ocean state represented by θ, as well as ice sheet coverage, the greenhouse gas level, and slow external radiative forcing (see Chapter 8).

11.4.3 Meridional Fluxes

Concerning the horizontal fluxes Q_T and Q_S represented by (11.22), Stommel (1961) makes the approximation

$$Q_T \approx Q_{\psi T} = |q_\psi| \delta T \tag{11.36a}$$

$$Q_S \approx Q_{\psi S} = |q_\psi| \delta S \tag{11.36b}$$

where $\delta T \equiv (T_e - T_p)$, $\delta S = (S_e - S_p)$, and q_ψ is the "volume exchange flux" at $y = L/2$ due to the TH circulation [i.e., the rate of water volume exchange, in Sverdrups (10^6 m^3 s^{-1}), across the latitude wall at $y = L/2$]. With the boundary conditions $\psi(D) = 0$, $\psi(D/2) = \psi_{max}$, the poleward part of the volume exchange (assumed to be positive in the upper branch of the circulation, as pictured in Fig. 10-3) is given by

$$\begin{aligned} q_\psi &= \int_0^W \int_{D/2}^D v \, dz \, dx \\ &= \int_0^W \int_{D/2}^D \frac{\partial \psi}{\partial z} dx \, dz \\ &= W \psi_{max} \end{aligned}$$

where ψ_{max} [$= (\psi_{max})_0$] is given by Eq. (11.35) and W is the width of the ocean basin. The absolute sign $|q|$ in Eq. (11.36) indicates that the flux of heat or salt is independent of the direction of the circulation between the boxes. Stommel (1961) identifies q_ψ as a pipelike loop connecting V_e and V_p (see Fig. 11-4).

More generally, however, in accordance with Eq. (10.22) the gyre flux contribution, Q_ϕ, and to a lesser extent the horizontal eddy flux, $Q^\star$, are also of importance, the

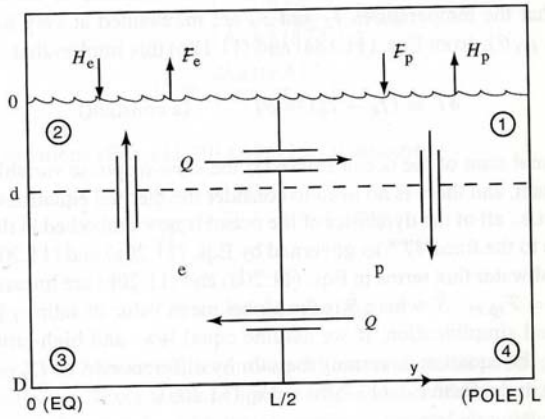

Figure 11-4 The two-box ocean system comprising a low-latitude box (e) and a polar box (p) connected by a volume exchange Q.

where, using Eqs. (11.30), (11.38), and (11.39),

$$q_\psi = k_\psi(\mu_T\,\delta T^* - \mu_S\,\delta S) \tag{11.41a}$$
$$q_\phi^\star = k_\phi \mu_T\,\delta T^* \tag{11.41b}$$

Thus, introducing Eq. (11.41) into Eq. (11.40) we obtain

$$\frac{V}{2}\frac{d(\delta S)}{dt} = \check{S}\mathcal{F}^\uparrow - K_S(\delta S)\cdot\delta S \tag{11.42a}$$

where the damping coefficient $K_S(\delta S)$ is given by,

$$\begin{aligned} K_S(\delta S) &= \left(k_\phi\mu_T|\delta T^*| + k_\psi|\mu_T\,\delta T^* - \mu_S\,\delta S|\right) \\ &= \mu_T|\delta T^*|\left[k_\phi + k_\psi\left(1 - \mu_S\,\delta S/\mu_T\,\delta T^*\right)\right] \end{aligned}$$

Note that for fixed values of $\mathcal{F}^\uparrow$ and δT^* a range of these values may exist wherein an increase of δS will weaken K_S to a point that allows a further increase of δS, i.e., a positive feedback that may give rise to an instability. As noted in Section 11.4.2 this would imply that δS would have to be considered a slow-response variable (see Section 6.1).
More formally, if we define the following nondimensional variables

$$s = \left(\frac{\mu_S}{\mu_T\,\delta T^*}\right)\delta S$$
$$(\Psi, \Phi) = \left(\frac{1}{k_\psi\mu_T\,\delta T^*}\right)(q_\psi, q_\phi^\star)$$
$$\Pi = \left[\frac{\mu_S\check{S}}{k_\psi\mu_T^2(\delta T^*)^2}\right]\mathcal{F}^\uparrow$$
$$t^* = \frac{2k_\psi\mu_T\,\delta T^*}{V}\,t$$

the governing equations [Eqs. (11.40) and (11.41)] become

$$\frac{ds}{dt^*} = \Pi - |\Psi|s - |\Phi|s \tag{11.42b}$$
$$\Psi = (1 - s) \tag{11.43a}$$
$$\Phi = (k_\phi/k_\psi) \equiv K_\phi \tag{11.43b}$$

The quantity Π is here considered to be an external parameter representing the ratio of the freshwater fluxes to the temperature gradient, which is a function of $y = (I, \mu, \theta; R, h, V, \mathcal{W})$ determined by the atmospheric general circulation via a GCM (see Chapter 7), but is not directly determined by the salinity gradient as measured by the free variable s. For any value of Π the steady-state (equilibria) of the system,

combination of which, denoted by $Q^{\star}_{\phi}$, we can also approximate in the form

$$Q^{\star}_{\phi(T,S)} \equiv \left[Q_{\phi(T,S)} + Q^{\star}_{(T,S)}\right] = \left|q^{\star}_{\phi}\right|\delta(T,S) \tag{11.37}$$

where $q^{\star}_{\phi}$ is the combined gyre/eddy volume exchange between V_{e} and V_{p}, which we shall assume is mainly due to the gyres with a smaller contribution due to the baroclinic eddies and smaller scale horizontal eddy mixing.

This volume exchange $q^{\star}_{\phi}$ is not forced by the salinity differences that contribute strongly to $\delta\rho$, but is forced in an indirect way by surface temperature differences and vertical heat fluxes that drive the atmospheric general circulation, including the surface wind systems. Thus, it is plausible to express $q^{\star}_{\phi}$ as a function only of the temperature difference, $\delta T = (T_{\mathrm{e}} - T_{\mathrm{p}})$, i.e.,

$$q^{\star}_{\phi} = \frac{k_{\phi}}{\rho^{*}}\,\mu_{\mathrm{T}}\delta T \tag{11.38}$$

where k_{ϕ} is a constant having the same units as k_{ψ}.

11.4.4 Dynamical Analysis of the Two-Box Model

The basic result concerning the potential instability and bimodality of the ocean can be demonstrated with the application of the following further simplifying approximations:

1. The geothermal flux $\mathcal{G}^{\uparrow}$ is neglected relative to the other terms in Eqs. (11.19a) and (11.19b).

2. The thermal restoring time scale $(V_n\Gamma^{-1})$ is assumed to be relatively short ($\sim$10 y) so that the temperatures T_{e} and T_{p} are maintained at very nearly the fixed values $T_{\mathrm{e,p}}(I, \mu, \theta)$; from Eqs. (11.18a) and (11.18b) this implies that

$$\delta T \equiv (T_{\mathrm{e}} - T_{\mathrm{p}}) \approx \delta T^{*} \qquad \text{(a constant)} \tag{11.39}$$

Thus the thermal state of the ocean is fixed if the slow-response variables I, μ, and θ are held constant, and there is no need to consider the thermal equations Eqs. (11.19a) and (11.19b); i.e., all of the dynamics of the ocean is now embodied in the way salinity varies relative to the fixed δT^{*} as governed by Eqs. (11.20a) and (11.20b).

3. The freshwater flux terms in Eqs. (11.20a) and (11.20b) are linearized by setting $\mathcal{F}_{(\mathrm{p,e})} \cdot \mathcal{S}_{(\mathrm{p,e})} = \mathcal{F}_{(\mathrm{p,e})} \cdot \breve{S}$, where $\breve{S}$ is the global mean value of salinity [Eq. (11.24)].

4. As a final simplification, if we assume equal low- and high-latitude volumes, $V_{\mathrm{e}} = V_{\mathrm{p}} \equiv V$, the equation governing the salinity difference $\delta S \equiv (S_{\mathrm{e}} - S_{\mathrm{p}}) \sim (-S_{\varphi})$ can be written in the form Eq. (11.20b) $-$ Eq. (11.20a):

$$\frac{V}{2}\,\frac{d(\delta S)}{dt} = \breve{S}\mathcal{F}^{\uparrow} - |q_{\psi}|\,\delta S - \left|q^{\star}_{\phi}\right|\,\delta S \tag{11.40}$$

Eqs. (11.42) and (11.43), governing s and hence the TH circulation Ψ via Eq. (11.43) are as follows:

1. When $s < 1$ (i.e., a "direct" thermally dominated TH circulation, $\Psi > 0$, with sinking cold dense water in high latitudes), two equilibria can exist if $\Pi < (1 + K_\phi)^2/4$,

$$s^{(1)} = \left(1 - \Psi^{(1)}\right) = \frac{1}{2}\left[(1 + K_\phi) - \sqrt{(1 + K_\phi)^2 - 4\Pi}\right]$$

$$s^{(2)} = \left(1 - \Psi^{(2)}\right) = \frac{1}{2}\left[(1 + K_\phi) + \sqrt{(1 + K_\phi)^2 - 4\Pi}\right]$$

2. When $s > 1$ (i.e., a reverse, salinity-dominated, TH circulation, $\Psi < 0$, with sinking salty water in low latitudes), an additional equilibrium exists for all $\Pi > K_\phi$,

$$s^{(3)} = \left(1 - \Psi^{(3)}\right) = \frac{1}{2}\left[(1 - K_\phi) + \sqrt{(1 - K_\phi)^2 + 4\Pi}\right]$$

The dependence of the equilibrium values of the TH circulation, $\Psi^{(n)}$, on the forcing Π is shown in Fig. 11-5, which is the bifurcation diagram for this ocean system (cf. Fig. 7-3 for the atmospheric EBM). By an eigenvalue analysis it is readily shown that $\Psi^{(1)}$ and $\Psi^{(3)}$ are stable (solid curves), separated by an unstable $\Psi^{(2)}$ (dashed line), with $\Psi^{(1)}$ and $\Psi^{(2)}$ merging at a "saddle node" when $\Pi = (1 + K_\phi)^2/4$ [see Section 6.3, Eq. (6.16), and Fig. 6-5a)]. The possibility for an instability and multiple

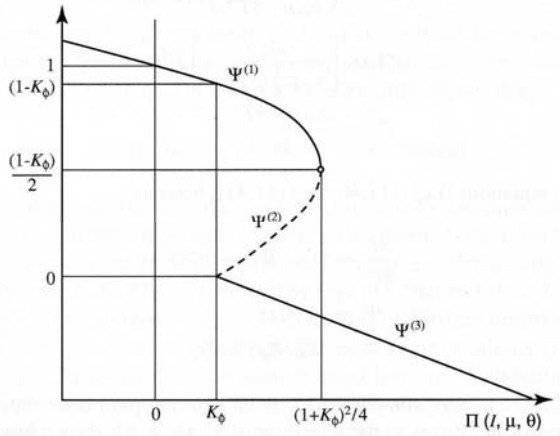

Figure 11-5 Bifurcation diagram showing the equilibrium values of the nondimensionalized volume flux by the TH circulation Ψ for the two-box ocean system, as a function of the "external" forcing function $\Pi(I, \mu, \theta)$.

equilibria of the ocean due to salinity, as illustrated by this simple model, is the central result of this analysis.

Thus, for the same value of forcing within the limits $K_\phi < \Pi < (1 + K_\phi)^2/4$ the system can admit stable equilibria either with a strong thermally direct circulation $\Psi > 0$ corresponding to a small salinity difference between equator and pole $s = (1 - \Psi)$, or another stable equilibrium with a weak direct circulation, $\Psi < 0$, associated with a large salinity difference. This latter salinity-dominated mode $\Psi^{(3)}$, which can be realized only if the salinity forcing can overcome the steady gyre flux, i.e., $\Pi > K_\phi$, might be identified with warm climatic periods of the past, e.g., the Cretaceous and Early Cenozoic when the Tethys Sea provided a large area of excess evaporation in low latitudes (see Figs. 3-1 and 3-3). This will be discussed further in Chapter 13 (Section 13.5).

The possible existence of multiple equilibria raises the question of possible rapid transitions between these modes as a factor in paleoclimatic change. Such transitions can arise as part of the more complete multivariable system involving ice and carbon dioxide, in the form of sustained oscillations, or can arise by slow forcing of Π to the bifurcation points $\Pi = K_\phi, (1+K_\phi)^2/4$, or by random forcing that causes a tunneling between $\Psi^{(1)}$ and $\Psi^{(3)}$. This latter possibility can be augmented by the "stochastic resonance" mechanism described in Chapter 7.

We note also that many two-dimensional zonal mean models and three-dimensional ocean models (OGCMs) have now been studied that can be tuned to replicate in greater detail these potential bimodal properties and reveal their sensitivity to atmospheric parameters. The first was made by Bryan (1986) and was followed, as examples, by Manabe and Stouffer (1988), Marotzke *et al.* (1988), Wright and Stocker (1991), and Fichefet and Hovine (1993). An example of a specific paleoceanographic application to glacial-maximum states was provided by Bigg *et al.* (1998). In Chapters 12 and 13 we discuss this possible role of ocean instability in a more time-dependent context as part of the fuller theory of paleoclimatic change.

At this point, it is worth emphasizing again that it is the ultimate role of the full-fledged OGCMs to include properly all of the coupled interactive circulation components that we have artificially separated for illustrative purposes. Such OGCMs form an essential component of a full time-dependent climate system model (CSM) as outlined at the beginning of Chapter 5 (see Fig. 5-1). However, we have also noted in that chapter that these more detailed models are still not capable of calculating the nonequilibrium net flux of heat across the ocean surface on the order of 10^{-1} W m^{-2}, as required by paleoclimatic observations of the variations of θ. Nor are these models able to account definitively for what is presently known about the grand circulation, and the subgrid-scale variability of the ocean, without the assignment of several free parameters. Thus, as we have said, it is not unreasonable to begin to approach the problem of paleoclimatic variations with the simplest models, which may require fewer free parameters than the more complex models. Moreover, these simpler models can at the least serve to illustrate the possibilities for long-term behavior, including possible instabilities that may ultimately be captured more rigorously by the full three-dimensional models.

Intermediate depth anomalies and the thermohaline circulation: toy models.

Pathways of MOW (I)

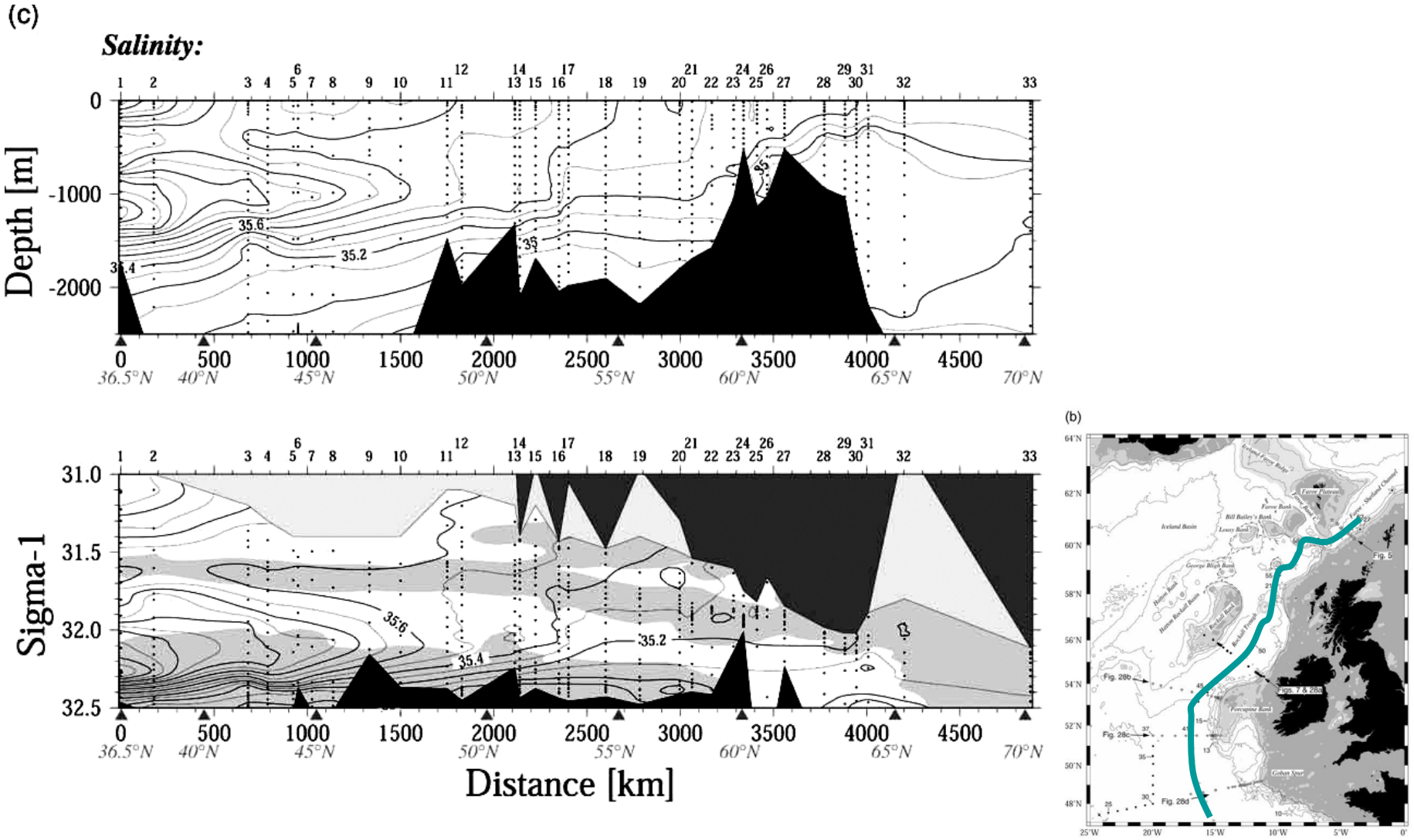

McCartney and Mauritzen, *Progr. Oceanogr.*, 2001.

Pathways of MOW (II)

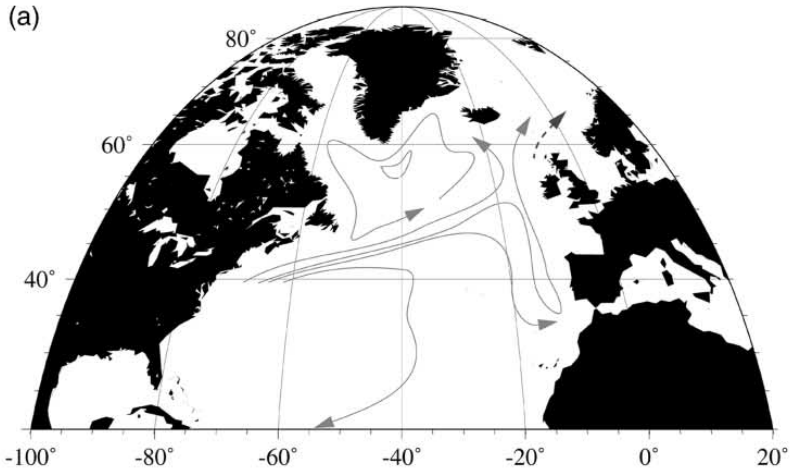

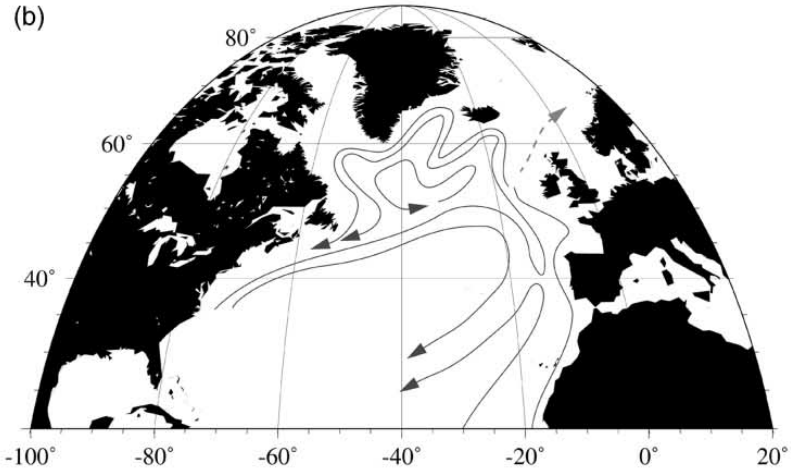

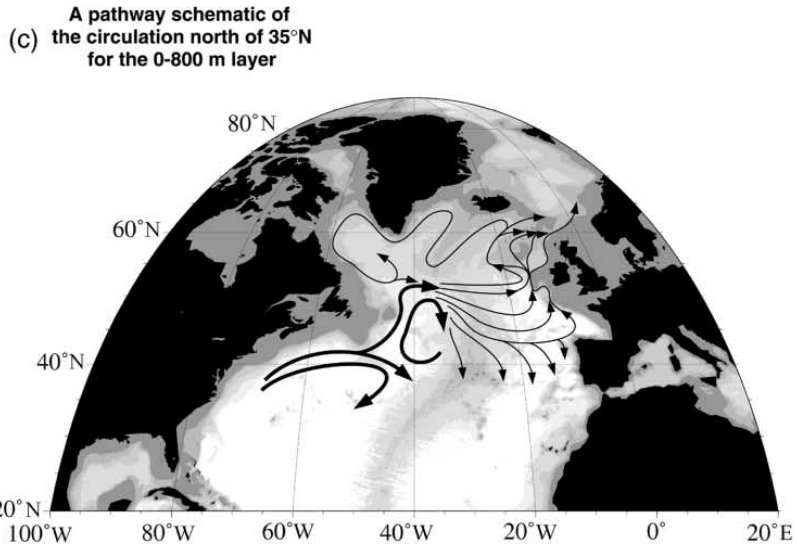

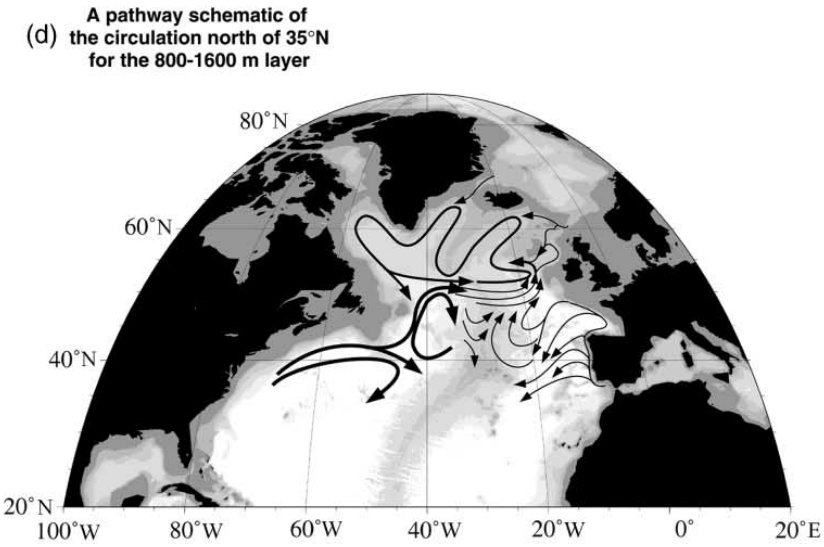

Pathways of MOW (III)

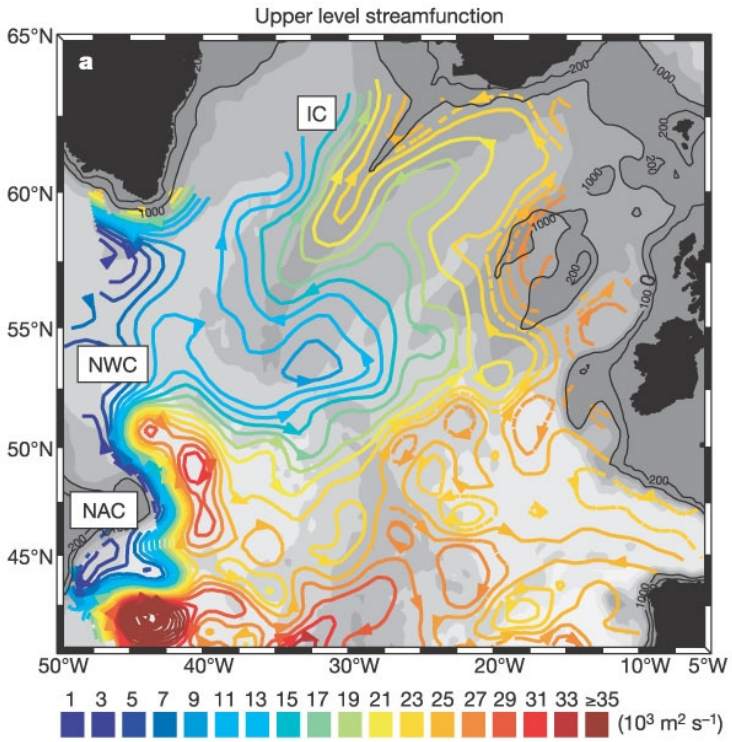

1000 m

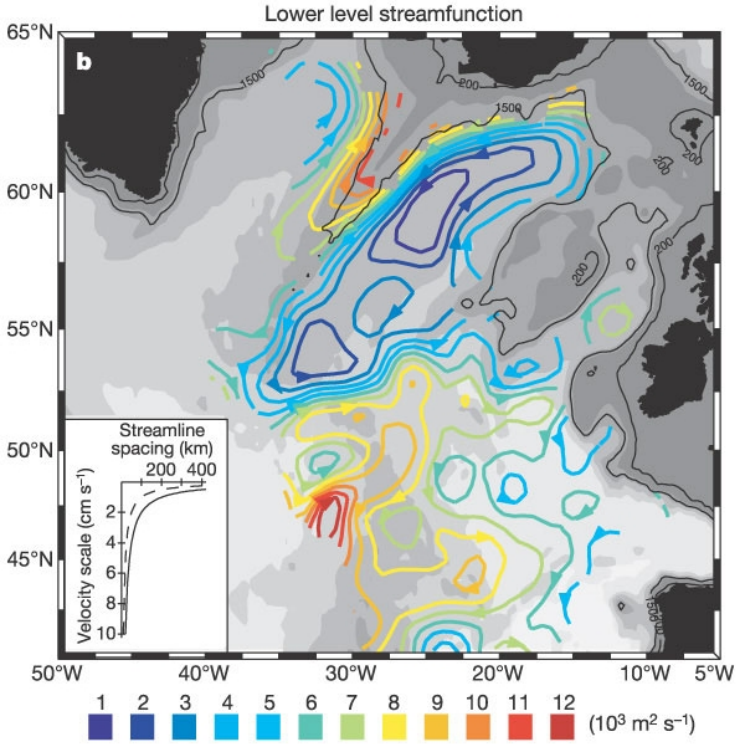

1500-1750m

Bower et al., *Nature*, 2002.

Stommel-type box-model to study the impact of MOW in the THC variability

We study three different scenario:

1) Standard (M0)
2) Outflow mixes with newly formed deep waters at high latitude (M6)
3) Outflow is carried to the surface layers by the large-scale circulation before entering the regions of deep-water formation (M5)

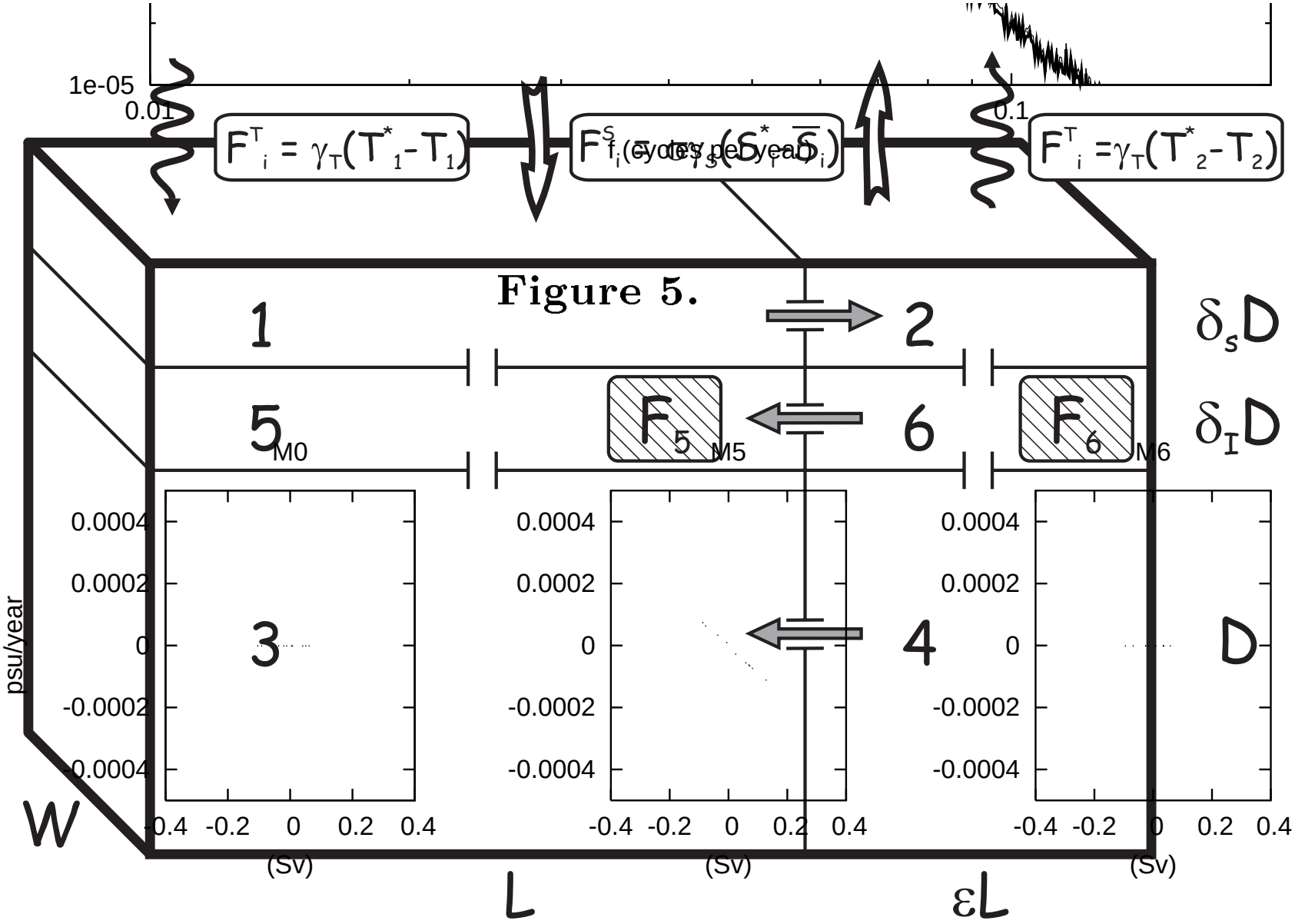

Figure 5.

Figure 6.

3 box-models with intermediate depth layer.

(M0)

(M5)

(M6)

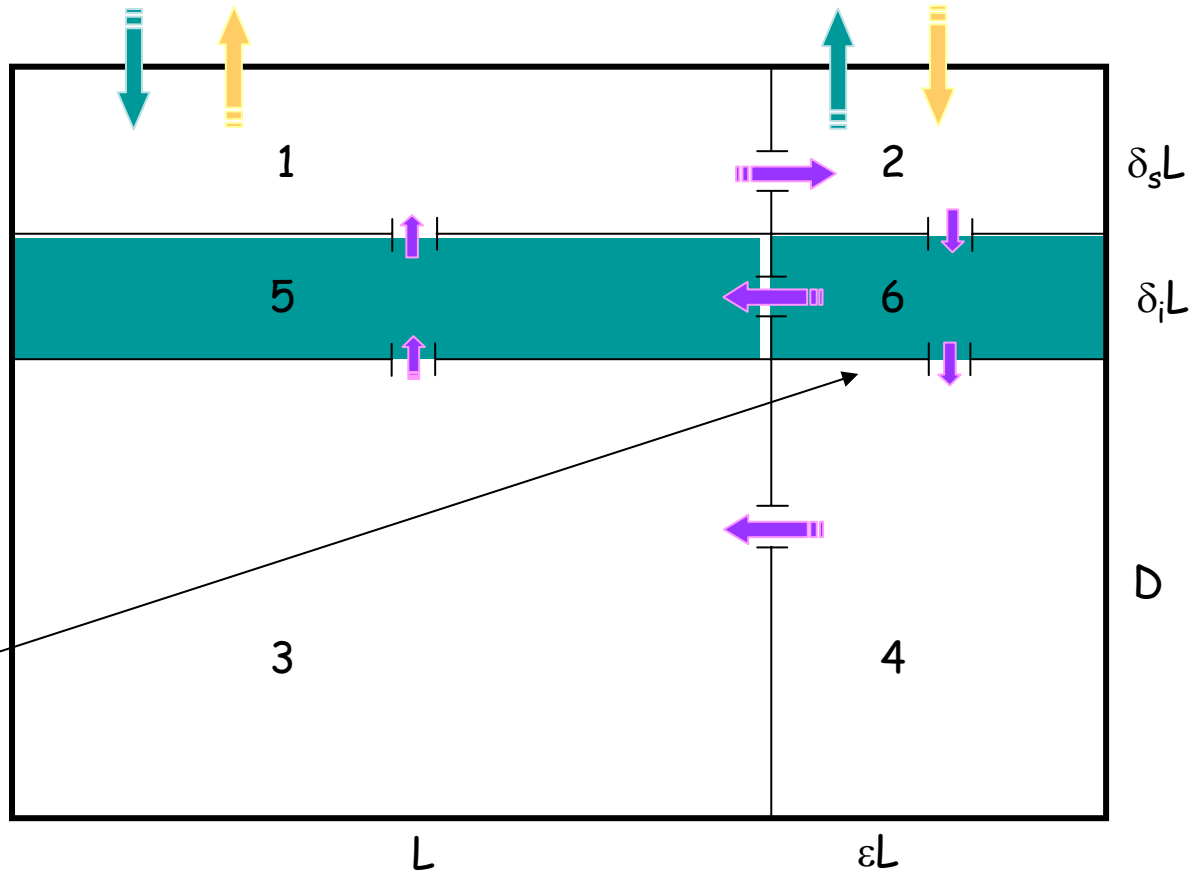

A box-model of the THC

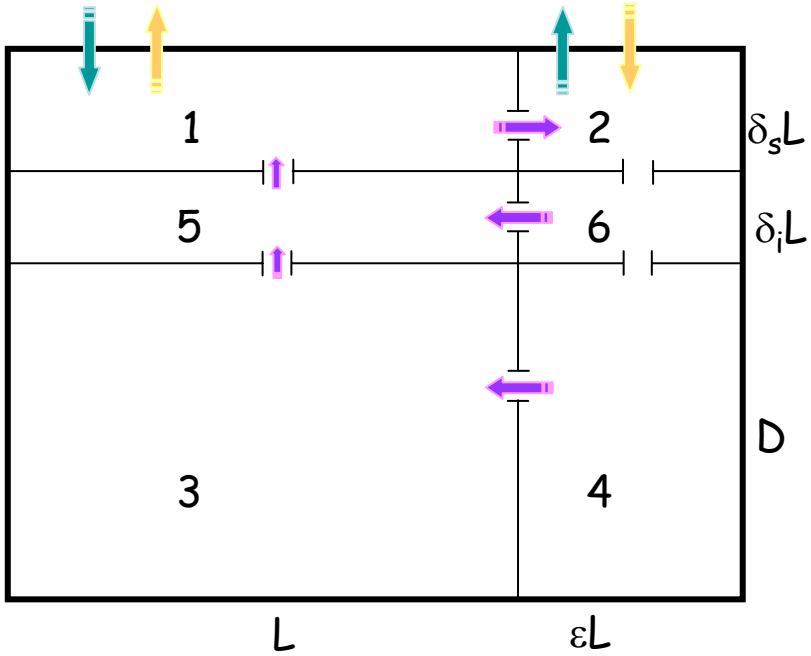

$$\dot{T}_1 = \frac{\Theta(U_{1-2})}{V}(T_5 - T_1) + \frac{\Theta(-U_{1-2})}{V}(T_2 - T_1) + \gamma_T(T_1^* - T_1),$$

$$\dot{T}_2 = \frac{\Theta(U_{1-2})}{\epsilon V}(T_1 - T_2) + \frac{\Theta(-U_{1-2})}{\epsilon V}(T_6 - T_2) + \gamma_T(T_2^* - T_2),$$

$$\dot{T}_3 = \frac{\Theta(U_{3-4})}{V}(T_5 - T_3) + \frac{\Theta(-U_{3-4})}{V}(T_4 - T_3),$$

$$\dot{T}_4 = \frac{\Theta(U_{3-4})}{\epsilon V}(T_3 - T_4) + \frac{\Theta(-U_{3-4})}{\epsilon V}(T_6 - T_3),$$

$$\dot{T}_5 = \frac{\Theta(-U_{1-2})\delta_S}{\delta_I V}(T_1 - T_5) + \frac{\Theta(-U_{5-6})}{V}(T_6 - T_5) + \frac{\Theta(-U_{3-4})}{\delta_I V}(T_3 - T_5),$$

$$\dot{T}_6 = \frac{\Theta(U_{1-2})\delta_S}{\epsilon\delta_I V}(T_2 - T_6) + \frac{\Theta(U_{5-6})}{\epsilon V}(T_5 - T_6) + \frac{\Theta(U_{3-4})}{\delta_I V}(T_4 - T_6).$$

and salinity:

$$\dot{S}_1 = \frac{\Theta(U_{1-2})}{V}(S_5 - S_1) + \frac{\Theta(-U_{1-2})}{V}(S_2 - S_1) + F_1$$

$$\dot{S}_2 = \frac{\Theta(U_{1-2})}{\epsilon V}(S_1 - S_2) + \frac{\Theta(-U_{1-2})}{\epsilon V}(S_6 - S_2) + F_2$$

$$\dot{S}_3 = \frac{\Theta(U_{3-4})}{V}(S_5 - S_3) + \frac{\Theta(-U_{3-4})}{V}(S_4 - S_3)$$

$$\dot{S}_4 = \frac{\Theta(U_{3-4})}{\epsilon V}(S_3 - S_4) + \frac{\Theta(-U_{3-4})}{\epsilon V}(S_6 - S_3)$$

$$\dot{S}_5 = \frac{\Theta(-U_{1-2})\delta_S}{\delta_I V}(S_1 - S_5) + \frac{\Theta(-U_{5-6})}{V}(S_6 - S_5) + \frac{\Theta(-U_{3-4})}{\delta_I V}(S_3 - S_5)$$

$$\dot{S}_6 = \frac{\Theta(U_{1-2})\delta_S}{\delta_I V}(S_2 - S_6) + \frac{\Theta(U_{5-6})}{V}(S_5 - S_6) + \frac{\Theta(U_{3-4})}{\delta_I V}(S_4 - S_6)$$

$$U_{1-2} = -\frac{\overline{U}}{\rho_0}[-(\rho_4 - \rho_3) - (\rho_6 - \rho_5)(2 + \delta_I)\delta_I - (\rho_2 - \rho_1)(1 + \delta_I)\delta_S],$$

$$U_{3-4} = -\frac{\overline{U}}{\rho_0}[(\rho_4 - \rho_3)(\delta_I + \delta_S) + (\rho_6 - \rho_5)(\delta_I + 2\delta_S)\delta_I + (\rho_2 - \rho_1)\delta_S^2],$$

$$U_{5-6} = -\frac{\overline{U}}{\rho_0}[-(\rho_4 - \rho_3) - (\rho_6 - \rho_5)(1 - \delta_S)\delta_I + (\rho_2 - \rho_1)\delta_S^2],$$

where

$$\overline{U} = \frac{gD}{\rho_0 r(1+\epsilon)(1+\delta_I+\delta_S)L}.$$

Steady states

- Sensitivity to fresh water parameter (sigma) introduced in the model equations computing the bifurcation diagram for the three model scenarios M0, M5 and M6, with sigma a control parameter

results

- For small sigma two steady solution exist
- As sigma grows a linear oscillatory eigenmode appears on the stable branch of solution
- M0, M5 and M6 are destabilized in correspondence with slightly different value

The linearized dynamics is computed numerically from the definition:

$$\mathbb{A}_{i,j} = \frac{[\mathbb{F}_i(x_1 \ldots x_j + \Delta x \ldots) - \mathbb{F}_i(x_1 \ldots x_j - \Delta x \ldots)]}{2\epsilon}, \tag{3}$$

where Δx has been set equal to 10^{-10}.

The behaviour of the system around the branch of stable solution is summarized in figure 4 by showing the real and imaginary components of the eigenvalues corresponding to the first unstable eigenvectors of A for the three model configurations , $M0$, $M5$ and $M6$. These are destabilized in correspondence with the following values of the control parameters σ:

$$\begin{aligned} M0 &\rightarrow \sigma_c = 1.211, \\ M5 &\rightarrow \sigma_c = 1.151, \\ M6 &\rightarrow \sigma_c = 1.234. \end{aligned}$$

Bifurcation diagram

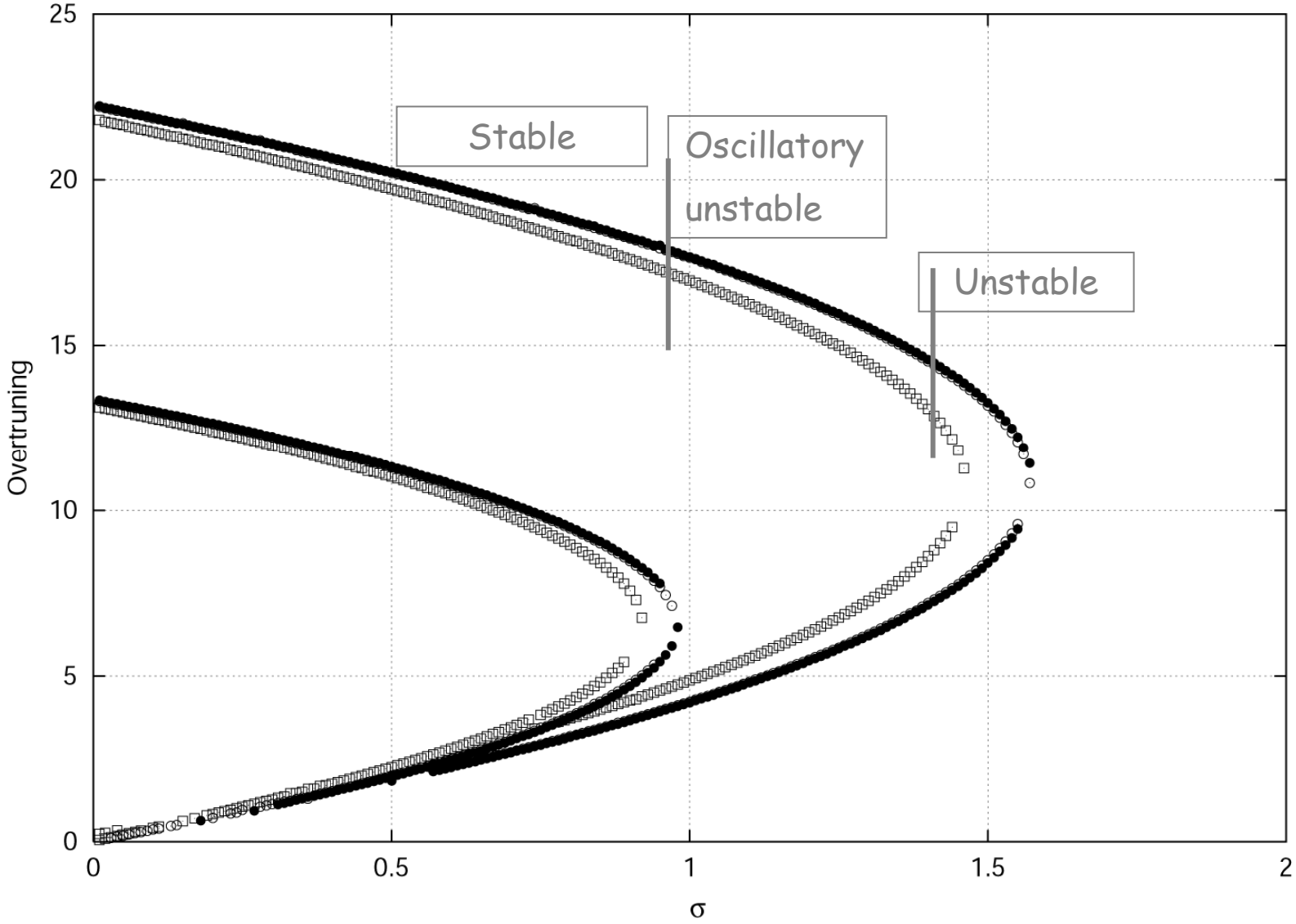

Linear stability

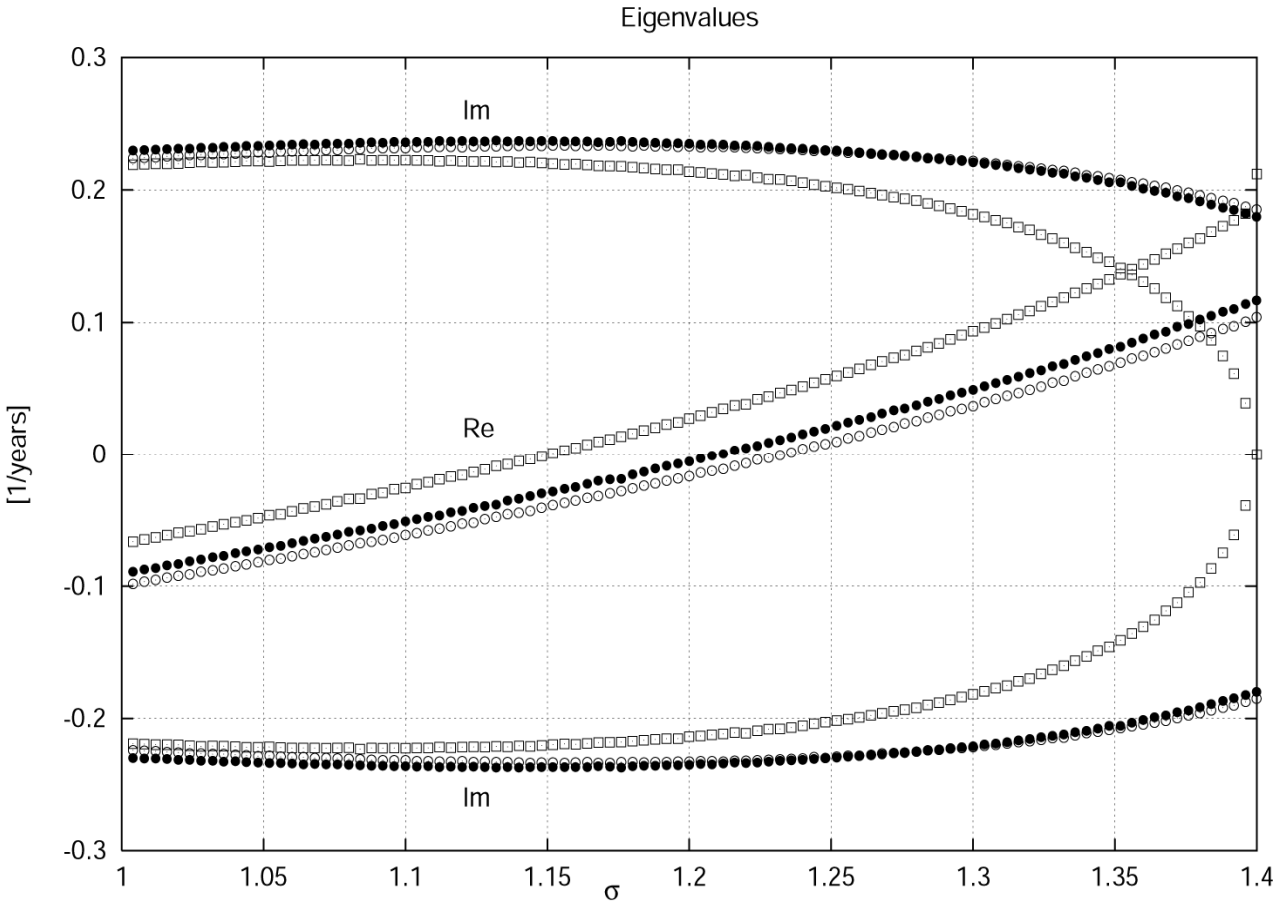

Advective feedback

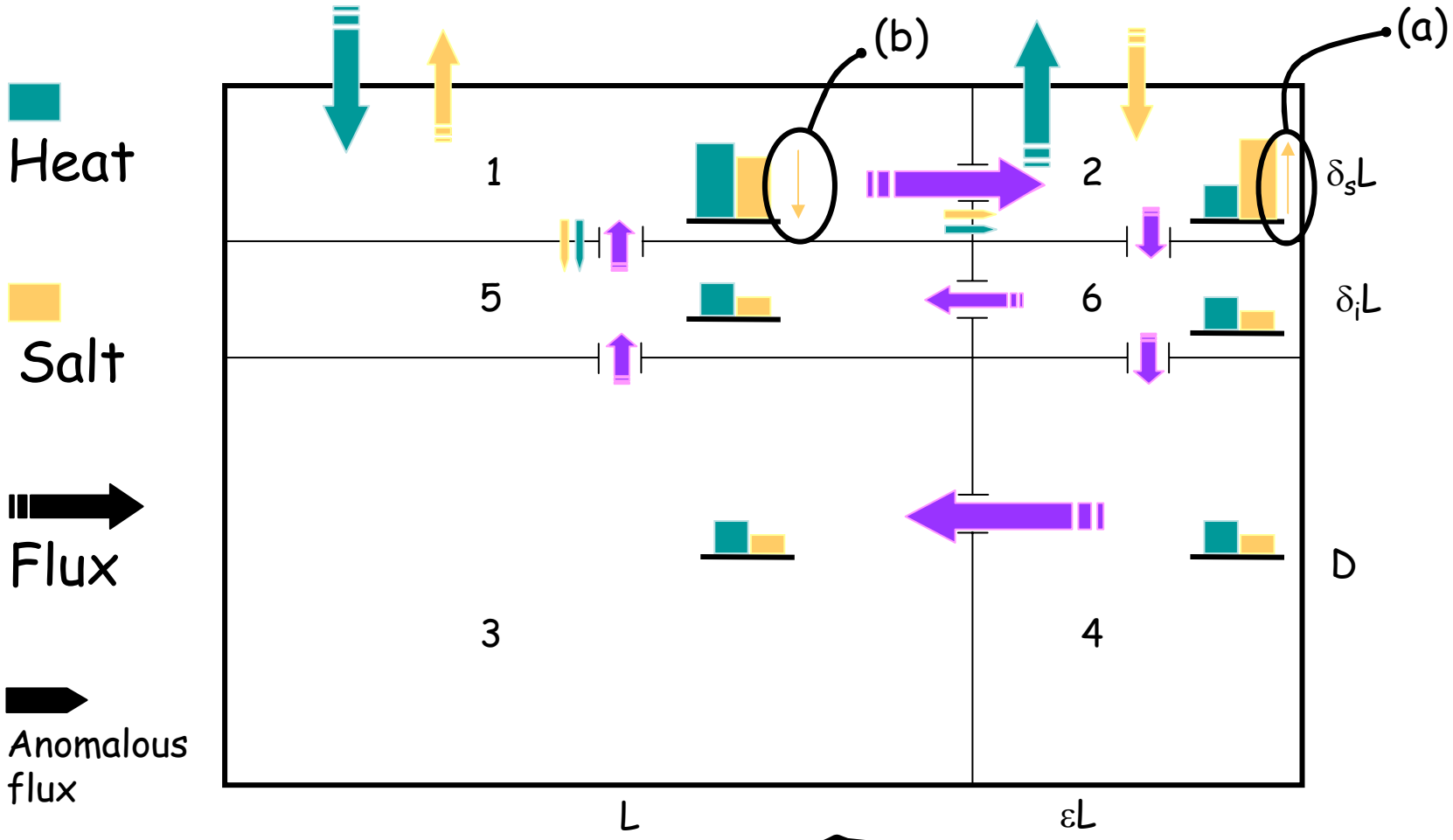

$(a) = U'_{1\text{-}2}\,(\underline{S}_5 - \underline{S}_1)$

$(b) = U'_{1\text{-}2}\,(\underline{S}_1 - \underline{S}_2)$

$b \approx \varepsilon\, a$

Positive feedback on the overturning

Only in the scenario M5 a salinity gradient is mainteined in the ocean interior

only

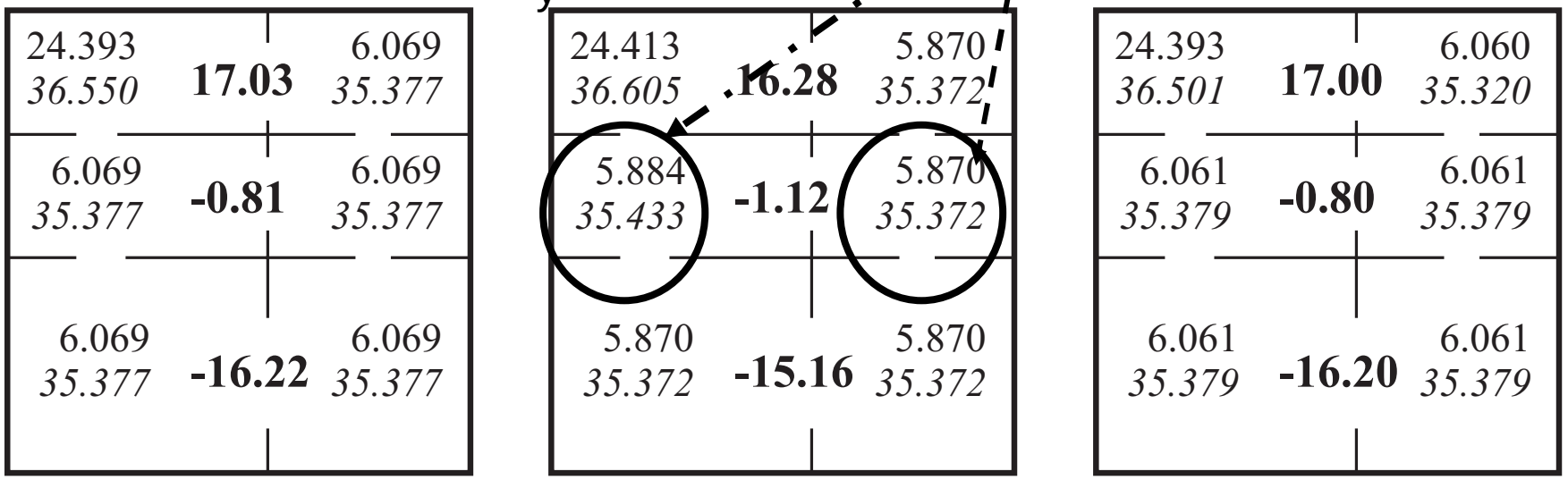

(a) (b) (c)

Stochastically forced oscillations

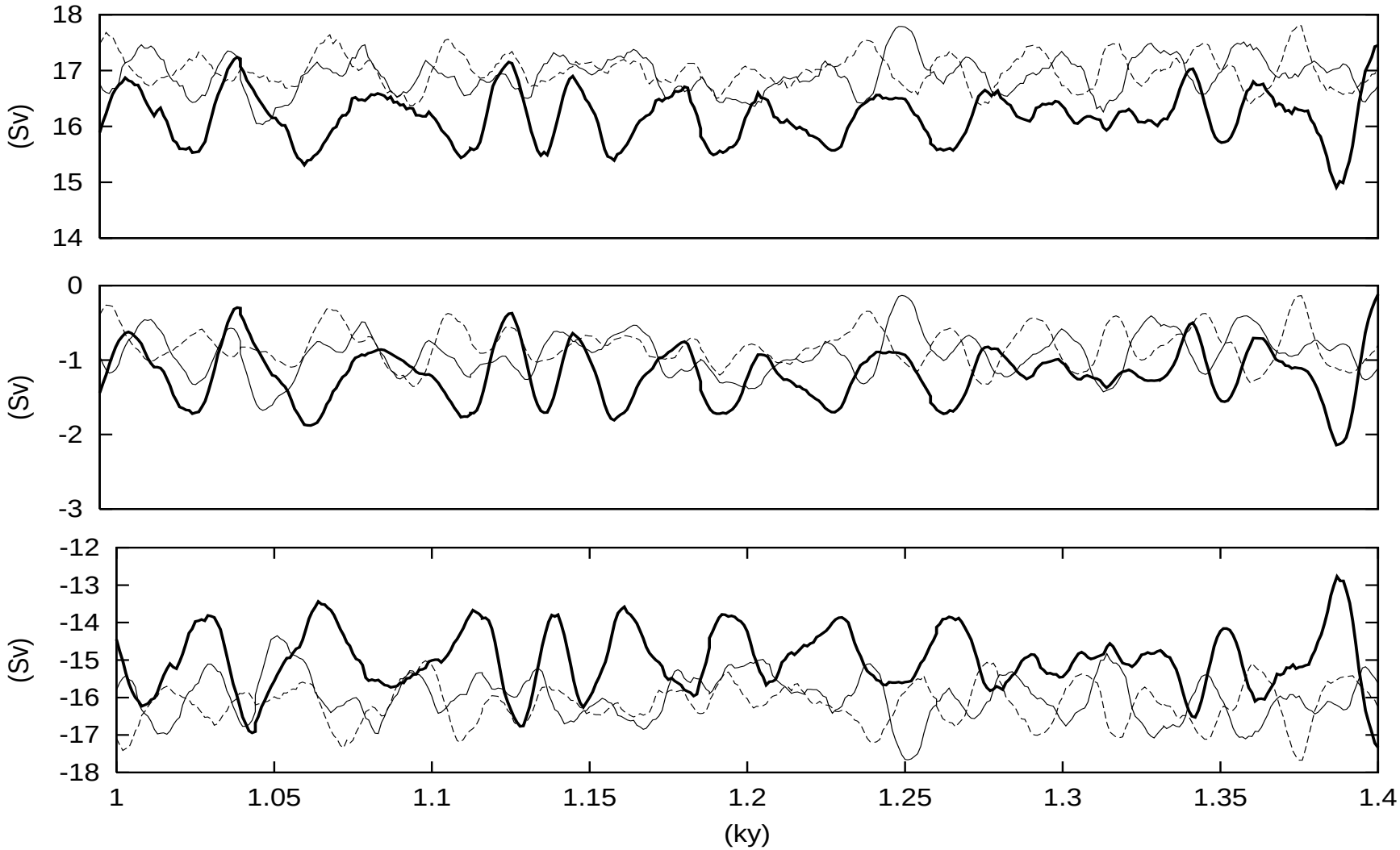

- Sampled stochastically sustained oscillation for scenario M0 (thin solid line), M5 (thick solid line), M6 (dashed line)
- Meridional transport ($U_{1\text{-}2}$) in the surface layer (top), $U_{5\text{-}6}$ in the intermediate layer (center) and $U_{3\text{-}4}$ in the deep layer (bottom) positive values corresponds to northward transport

Average power spectra of U_{1-2}

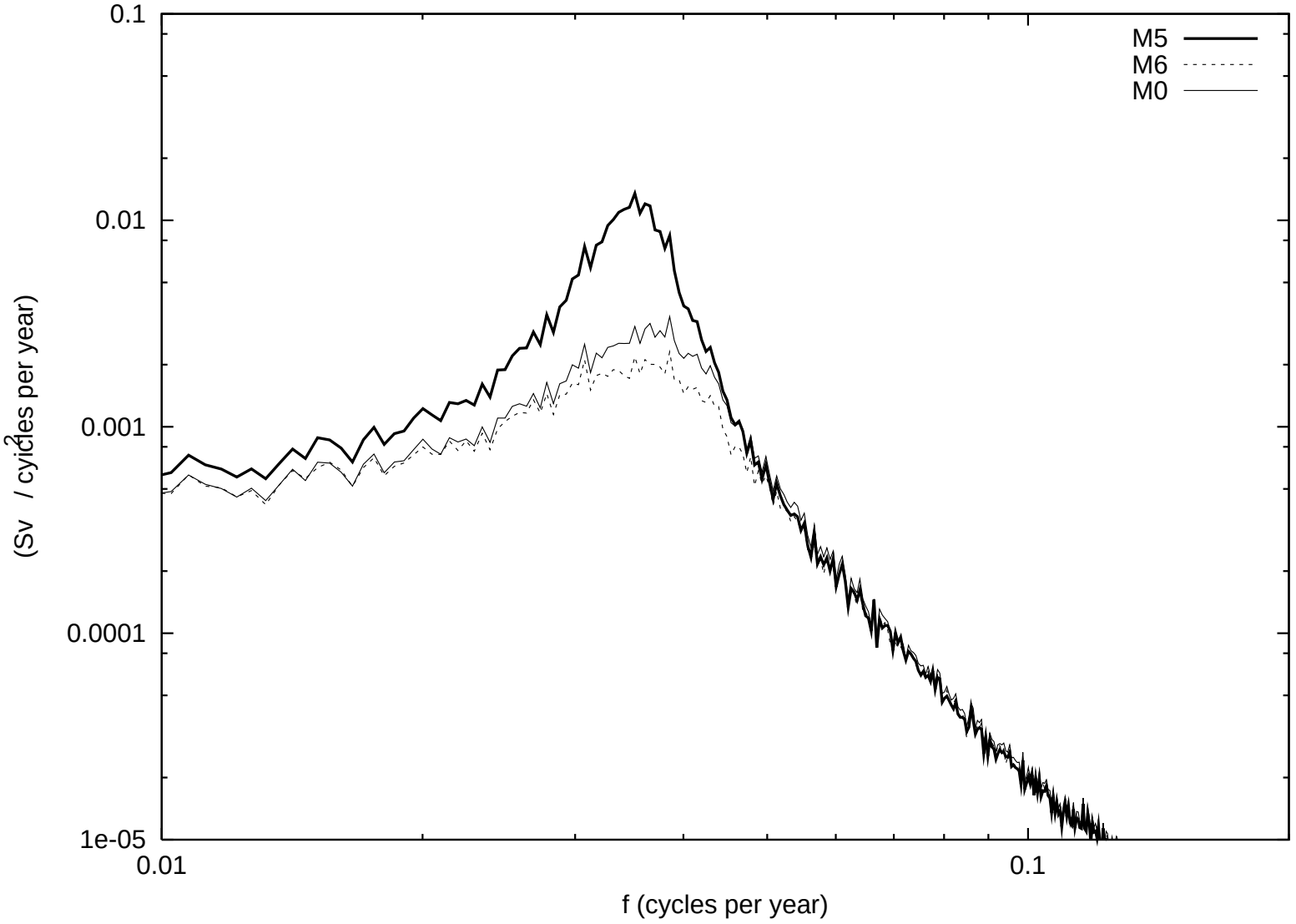

A 2-D model of the THC

$$\frac{\partial \xi^*}{\partial t^*} + J^*(\xi^*, \psi^*) = Ra \frac{\partial}{\partial y^*}(T^* - \lambda S^*) + Pr^{-1/2} \frac{\partial^2 \xi^*}{\partial y^{*2}} + r_v \, Pr^{-1/2} \frac{\partial^2 \xi^*}{\partial z^{*2}}$$

$$\delta^2 \frac{\partial^2 \psi^*}{\partial y^{*2}} + \frac{\partial^2 \psi^*}{\partial z^{*2}} = -\xi$$

$$\frac{\partial T^*}{\partial t^*} + J^*(T^*, \psi^*) = Pr^{1/2} \frac{\partial^2 T^*}{\partial y^{*2}} + r_d \, Pr^{1/2} \frac{\partial^2 T^*}{\partial z^{*2}}$$

$$\frac{\partial S^*}{\partial t^*} + J^*(S^*, \psi^*) = Pr^{1/2} \frac{\partial^2 S^*}{\partial y^{*2}} + r_d \, Pr^{1/2} \frac{\partial^2 S^*}{\partial z^{*2}}$$

where:

$$Ra = \frac{g\alpha \overline{T} D L^2}{k_H \nu_H}, \qquad \lambda = \frac{\beta \overline{S}}{\alpha \overline{T}}, \qquad Pr = \frac{k_H}{\nu_H},$$

$$\delta = \frac{D}{L}, \qquad r_v = \frac{\nu_V}{\delta^2 \nu_H}, \qquad r_d = \frac{k_V}{\delta^2 k_H}.$$

$$\psi = 0, \quad \xi = 0, \qquad \frac{\partial (S,T)}{\partial n} = 0, \qquad T(y,0) = \frac{1}{2}\cos(2\pi y), \qquad \frac{\partial S}{\partial z}(y,0) = \sigma_e g(y).$$

Free-slip Closed basin Mixed boundary conditions

Stationary states in a symmetric 2-D model of the THC

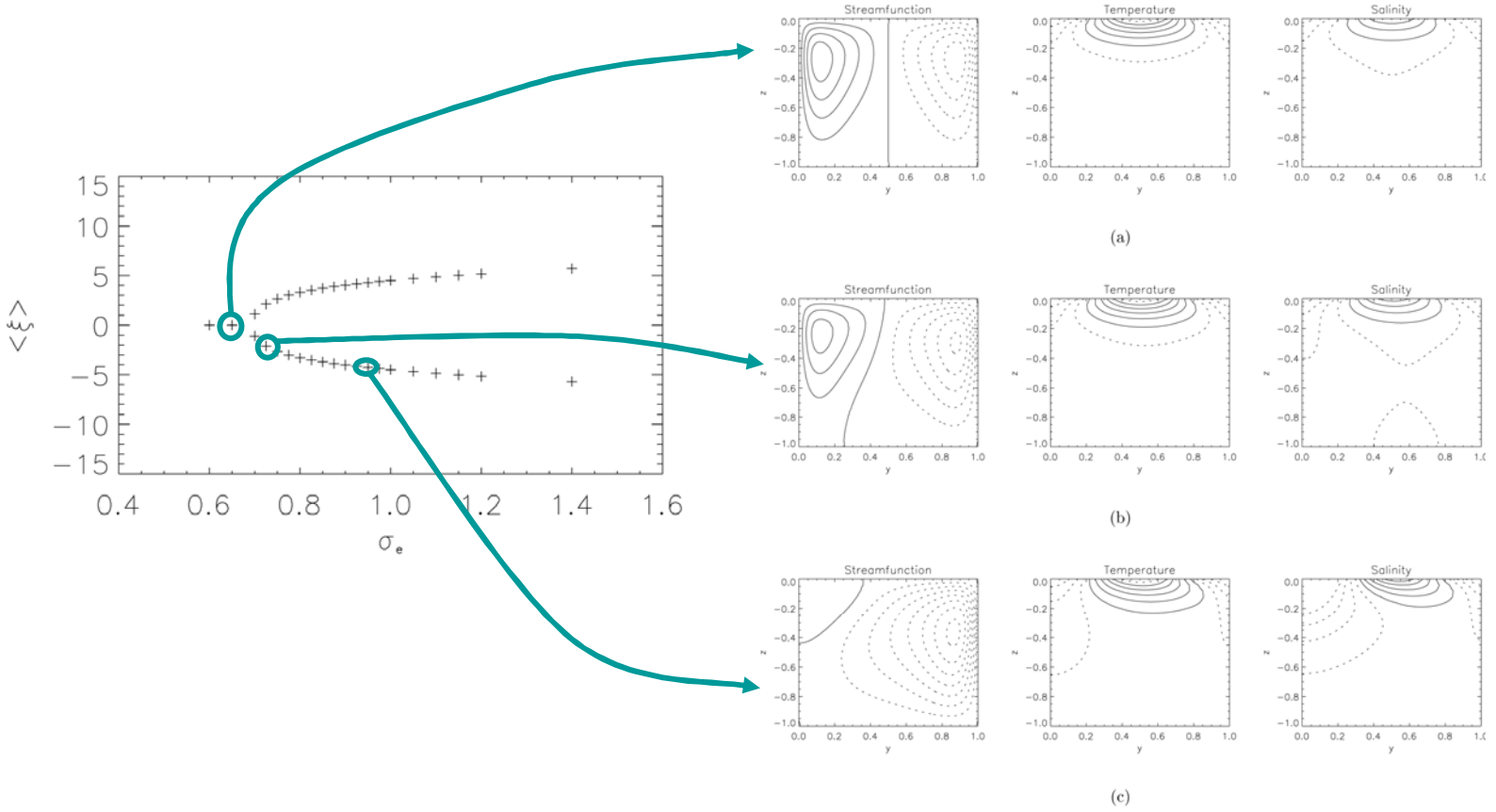

Artale et al., *Tellus,* 2002

Model sensitivity to k_v

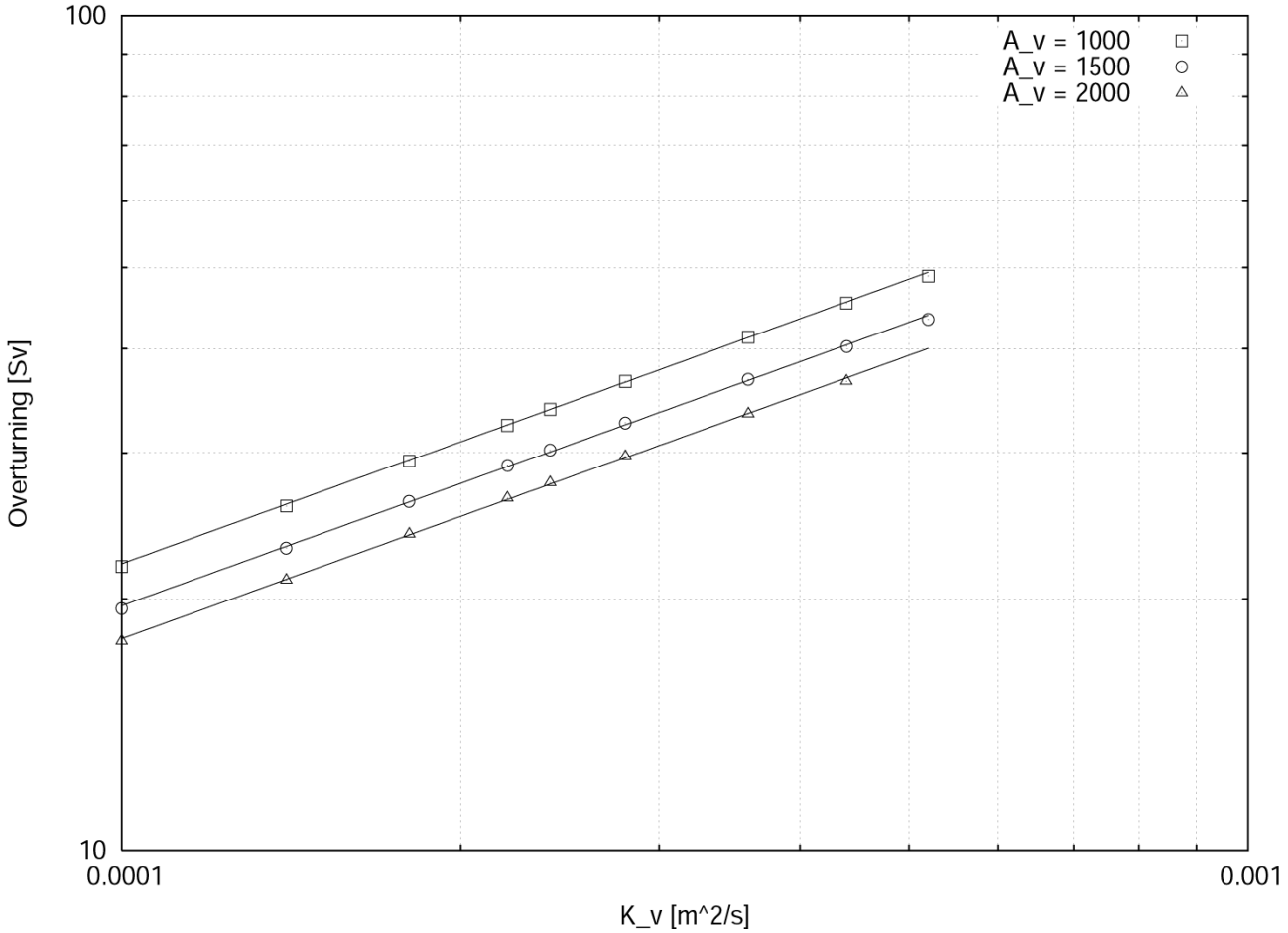

Intermediate Depth anomalies in a symmetric in the THC

$$\frac{\partial T}{\partial t} + J(T,\psi) = Pr^{1/2}\frac{\partial^2 T}{\partial y^2} + \tau_d Pr^{1/2}\frac{\partial^2 T}{\partial z^2} + \theta_i s(y,z),$$

$$\frac{\partial S}{\partial t} + J(S,\psi) = Pr^{1/2}\frac{\partial^2 S}{\partial y^2} + \tau_d Pr^{1/2}\frac{\partial^2 S}{\partial z^2} + \sigma_i s(y,z).$$

Where σ_i and θ_i are the amplitude of the temperature and salinity anomalies, $s(y,z)$ is a shape function which we set as:

$$s(y,z) = \frac{1}{A_0} e^{-\frac{(x-x_0)^2}{w^2}} e^{-\frac{(z-z_0)^2}{a^2}},$$

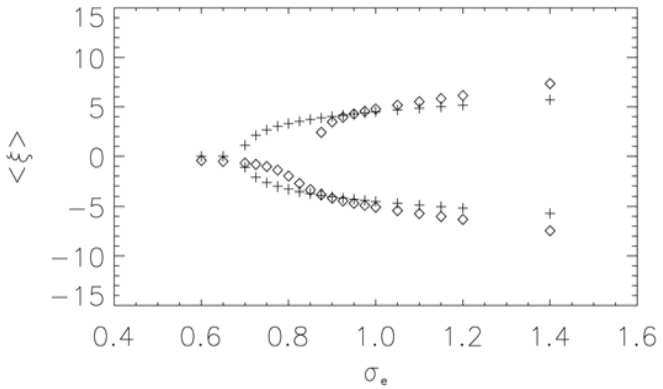

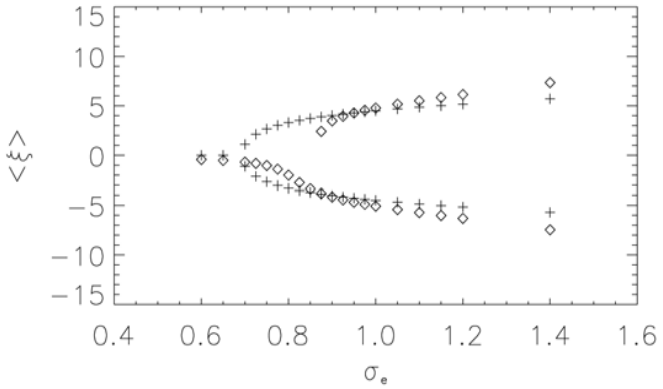

Advective feedback in a in a 2-D model of the THC

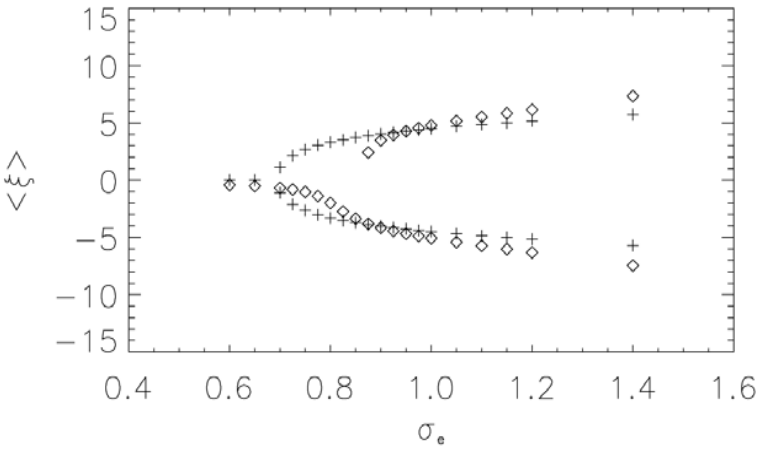

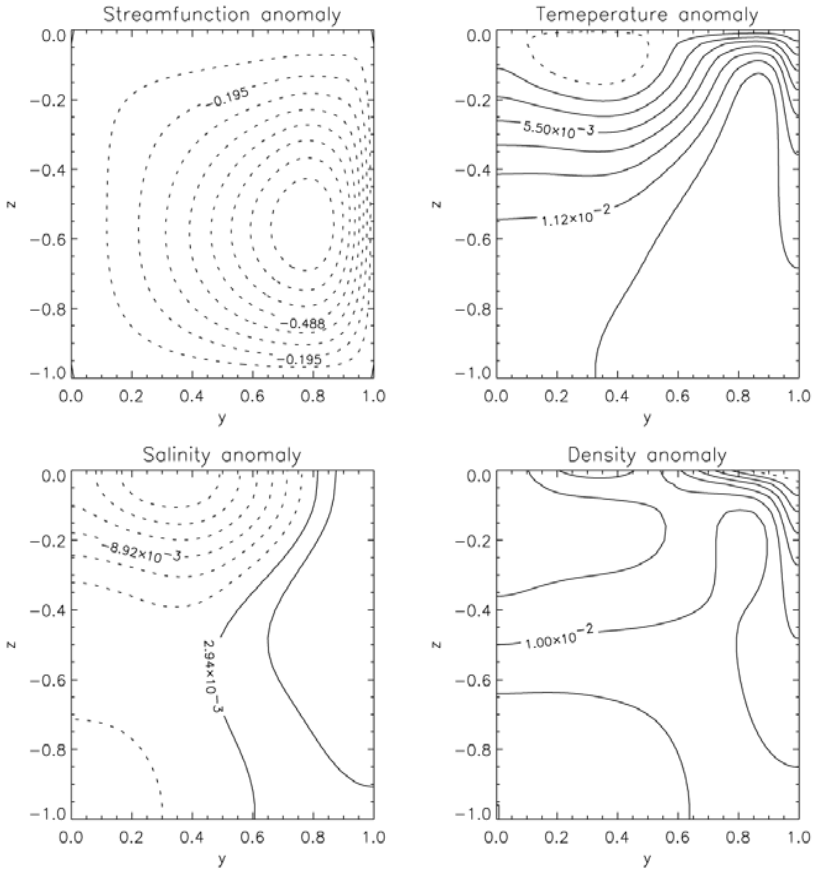

Artale et al.,
Tellus, 2002.

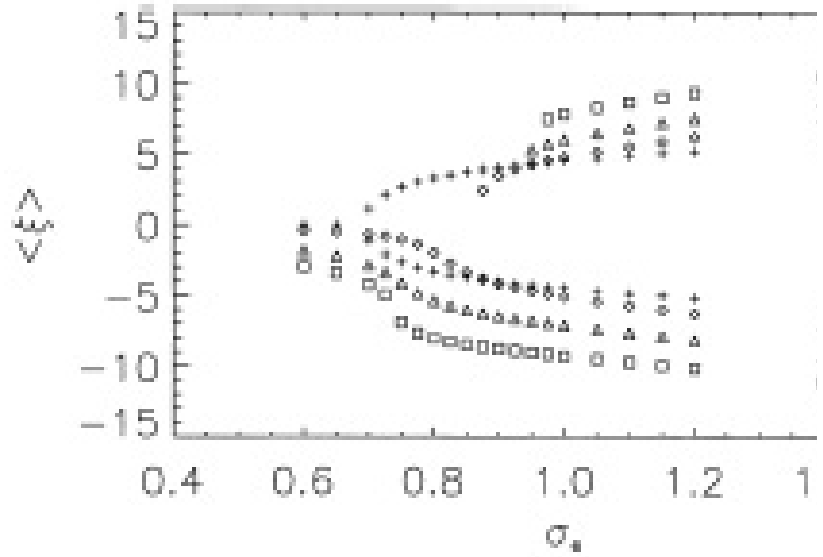

Fig. 6. Bifurcation diagrams corresponding to different strength of the internal anomaly: $\sigma_i = 0.5$ (diamonds); $\sigma_i = 2.5$ (triangles); $\sigma_i = 5.0$ (squares).

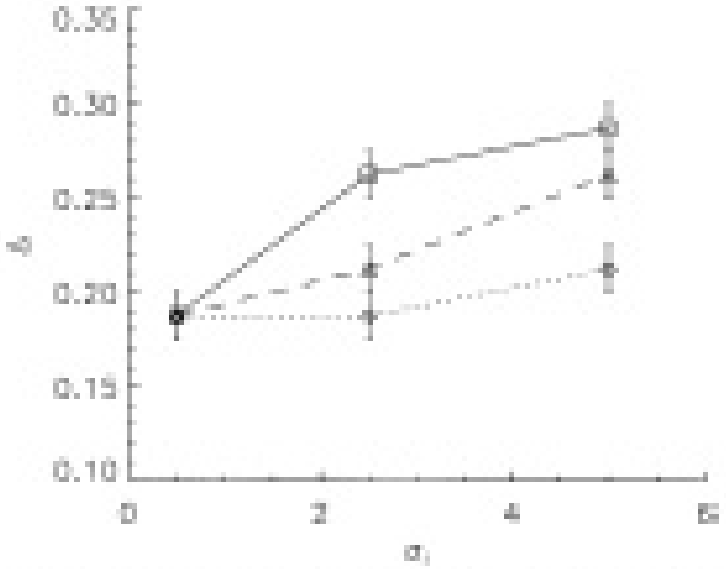

Fig. 7. The interval Δ between the pitchfork bifurcation obtained with the symmetric setup and the limit point on the SPF branch as a function of the strength of the internal anomaly. The dependence is shown for the internal anomaly centered at different heights: $z_0 = 3/4$ (squares); $z_0 = 1/2$ (triangles); $z_0 = 1/4$ (diamonds).

2 Conceptual model of the Atlantic conveyor belt

In this section, a conceptual model of the thermohaline circulation is introduced which extends Stommel's box model to cross-hemispheric flow, making it directly applicable to NADW formation (Fig. 1). This is similar to the models discussed by Rooth (1982) and Marotzke

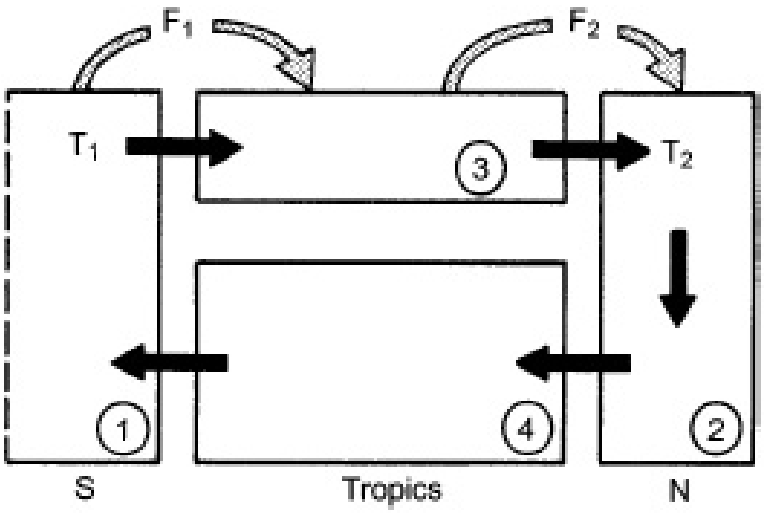

Fig. 1. A simple 4-box model of cross-hemispheric thermohaline flow. North Atlantic Deep Water forms in box *2*; its outflow towards box *1* is controlled by the density difference between boxes *2* and *1*. Salinities in the boxes are determined by the flow and the surface freshwater fluxes entering boxes *1*, *2* and *3*. Only two of these three fluxes are independent, since their sum must vanish in a steady state. Therefore the surface freshwater fluxes are portrayed as two atmospheric vapour transports F_1 and F_2, whose significance is discussed in the text

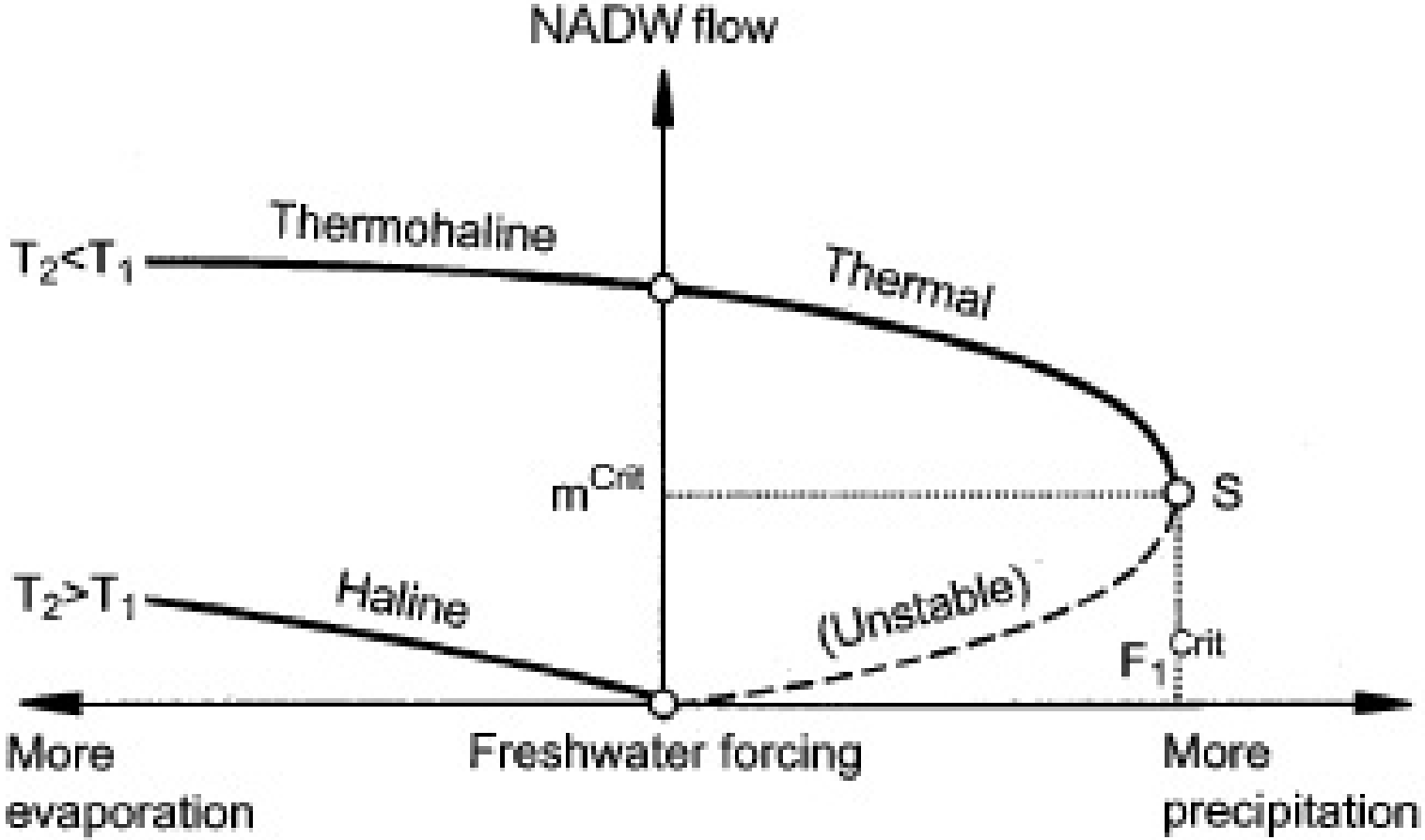

Fig. 2. The three flow regimes (*solid*) of the box model. The *dashed line* is an unconditionally unstable solution. *S* is the saddle-node bifurcation point

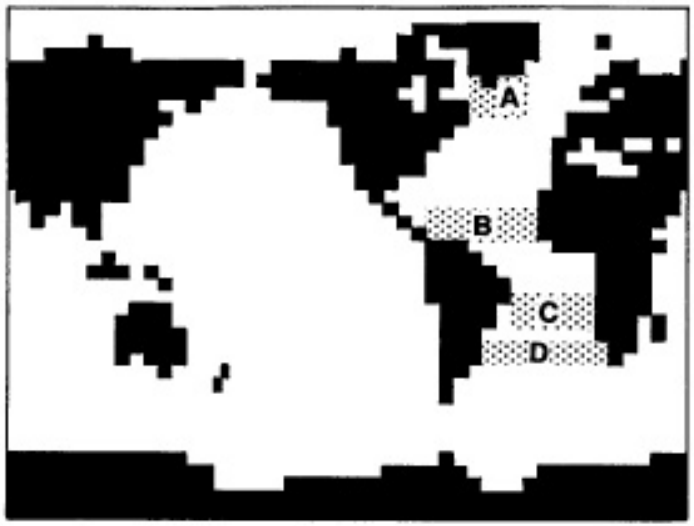

Fig. 4. A map of the four different regions where freshwater forcing was perturbed by adding a slowly increasing flux. Global mean salinity was conserved by an opposite perturbation in the equatorial Pacific

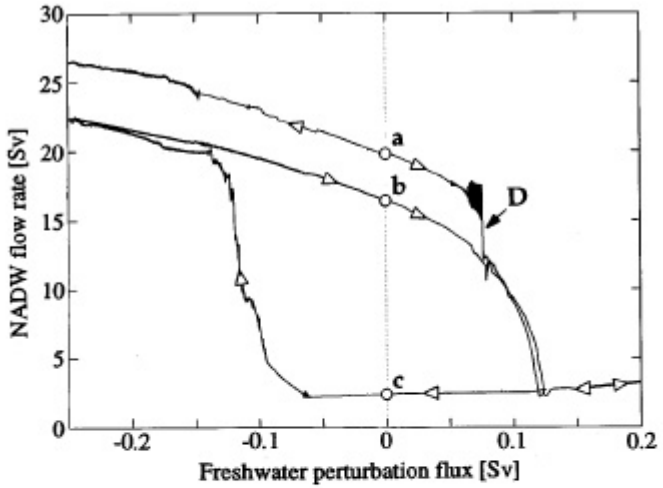

Fig. 5. Hysteresis response of the North Atlantic overturning to a slowly changing freshwater forcing (at a rate of 0.05 Sv/1000 y) in region *B*. Point *a* is the initial equilibrium state; from there the freshwater forcing was gradually increased until the *right edge* of the figure was reached, then decreased again moving through point *c* towards the *left edge*, then increased once more through point *b*. *Open circles* mark true equilibria as confirmed by continuing the integration with constant freshwater forcing for several thousand years. Point *b* is thus the final equilibrium reached after one (clockwise) hysteresis loop; it differs from *a* by the absence of Labrador Sea convection. Point *c* is a state with no NADW formation and all deep water forming in the Southern Hemisphere